DISEASES AND DISORDERS

Glucocorticoid-induced loss of beneficial gut bacterial extracellular vesicles is associated with the pathogenesis of osteonecrosis

Chun-Yuan Chen[1,2], Shan-Shan Rao[2,3], Tao Yue[1,2], Yi-Juan Tan[1,2], Hao Yin[1,2], Ling-Jiao Chen[4], Ming-Jie Luo[2,3], Zun Wang[2,3], Yi-Yi Wang[1,2], Chun-Gu Hong[2], Yu-Xuan Qian[1,2], Ze-Hui He[1,2], Jiang-Hua Liu[1,2], Fei Yang[5], Fei-Yu Huang[5], Si-Yuan Tang[3], Hui Xie[1,2,6,7,8,9]*

Osteonecrosis of the femoral head (ONFH) commonly occurs after glucocorticoid (GC) therapy. The gut microbiota (GM) participates in regulating host health, and its composition can be altered by GC. Here, this study demonstrates that cohousing with healthy mice or colonization with GM from normal mice attenuates GC-induced ONFH. 16*S* rRNA gene sequencing shows that cohousing with healthy mice rescues the GC-induced reduction of gut *Lactobacillus animalis*. Oral supplementation of *L. animalis* mitigates GC-induced ONFH by increasing angiogenesis, augmenting osteogenesis, and reducing cell apoptosis. Extracellular vesicles from *L. animalis* (*L. animalis*-EVs) contain abundant functional proteins and can enter the femoral head to exert proangiogenic, pro-osteogenic, and antiapoptotic effects, while its abundance is reduced after exposure to GC. Our study suggests that the GM is involved in protecting the femoral head by transferring bacterial EVs, and that loss of *L. animalis* and its EVs is associated with the development of GC-induced ONFH.

INTRODUCTION

Osteonecrosis of the femoral head (ONFH) is a painful, refractory, and debilitating bone disease that often occurs in patients receiving systemic glucocorticoid (GC) therapy (*1*, *2*). The gradually progressive death of bone cells (osteocytes, osteoblasts, osteoclasts, etc.) and bone marrow is the main pathological feature of this disease, which eventually leads to femoral head structural changes or even collapse and hip joint destruction (*3*). GC-induced inhibition of osteogenesis and promotion of bone cell apoptosis contribute importantly to the pathogenesis of ONFH (*1*, *4*). GC also disrupts skeletal angiogenesis and induces endothelial damage, thereby reducing blood supply to the femoral head and lastly resulting in bone cell death and bone architecture destruction (*5*, *6*). Nevertheless, the impact of GC is systemic, and the GC-induced alteration of other processes may be also involved in the development of ONFH.

The gut microbiota (GM) has been identified as an important symbiotic partner in the maintenance of animal and human health (*7*). The composition and diversity of GM can be altered by multiple host-intrinsic (e.g., age, host health status, and genetics) and host-extrinsic (e.g., lifestyle, drug usage, and diet) factors, which may disturb physiological homeostasis in the host and lead to various diseases, such as Alzheimer's disease (*8*), inflammatory bowel disease (*9*), and cancer (*10*). Recent evidence has also shown associations between bone homeostasis and GM. Li *et al.* (*11*) have found that estrogen deprivation–induced bone loss is GM dependent and can be attenuated by feeding of *Lactobacillus rhamnosus* GG, a well-studied and commonly recommended probiotic strain, or VSL#3, a commercially available probiotic cocktail that comprises eight strains of lactic acid–producing bacteria. The difference in bone mass between conventional and germ-free mice also indicates the involvement of GM in the regulation of bone health (*12*, *13*). Wei *et al.* (*14*) have shown that the oral bacterial population is different in patients with bisphosphonate-related osteonecrosis of the jaw and individuals without this disease. Currently, however, there is no evidence that uncovers the role of GM in the development of GC-induced osteonecrosis. Studies have revealed that the exogenous administration of GC can result in structural changes of GM in both humans and animals (*15*, *16*). Considering the regulatory effect of GM on bone, we hypothesized that GC-induced gut dysbiosis might be a critical factor associated with the pathogenesis of ONFH.

Extracellular vesicles (EVs) are nanosized membrane-enclosed particles that play a crucial role in short- and long-distance intracellular communication in both prokaryotic and eukaryotic cells by selectively transferring donor cell–derived bioactive molecules to recipient cells (*17*–*19*). Release of EVs—a common feature of Gram-negative bacteria and also found in some Gram-positive bacteria, which promotes bacterial survival and also enables bacteria to communicate with host cells by delivering their cargos to host cells for modulating host function (*20*–*22*). It has been reported that GM-derived EVs from mice on high-fat diets exhibit increased abundance of EVs secreted by *Pseudomonas panacis* compared to those from normal diet–fed mice (*23*). After oral administration, *P. panacis*–EVs can enter the mouse systemic circulation and then the insulin-responsive organs to elicit insulin resistance and impair glucose metabolism (*23*). This study presents a new bacterial EV–mediated mode of intercellular cross-talk between the GM and the host. To date, evidence is lacking on whether GM can affect bone homeostasis in

[1]Department of Orthopaedics, Xiangya Hospital, Central South University, Changsha, Hunan 410008, China. [2]Movement System Injury and Repair Research Center, Xiangya Hospital, Central South University, Changsha, Hunan 410008, China. [3]Xiangya School of Nursing, Central South University, Changsha, Hunan 410013, China. [4]Department of Pathology, Sun Yat-sen Memorial Hospital, Sun Yat-sen University, Guangzhou, Guangdong 510220, China. [5]Department of Occupational and Environmental Health, Xiangya School of Public Health, Central South University, Changsha, Hunan 410078, China. [6]Department of Sports Medicine, Xiangya Hospital, Central South University, Changsha, Hunan 410008, China. [7]Hunan Key Laboratory of Organ Injury, Aging and Regenerative Medicine, Changsha, Hunan 410008, China. [8]Hunan Key Laboratory of Bone Joint Degeneration and Injury, Changsha, Hunan 410008, China. [9]National Clinical Research Center for Geriatric Disorders, Xiangya Hospital, Central South University, Changsha, Hunan 410008, China.
*Corresponding author. Email: huixie@csu.edu.cn

the femoral head through the transfer of specific bacterium-derived EVs.

Here, we explored whether cohousing with healthy mice or colonization with GM from normal mice could protect the femoral head from GC-induced osteonecrosis. Subsequently, we used 16*S* ribosomal RNA (rRNA) gene sequencing to screen the candidate bacteria that might be associated with GC-induced ONFH and tested whether transplantation with the candidate bacteria could affect GC-induced ONFH in mice. Last, we determined whether EVs from the specific gut bacteria could enter the femoral head to exert regulatory effects on bone microarchitecture, osteogenesis, angiogenesis, and cell apoptosis in the GC-treated mice. Meanwhile, we used proteomic analysis to identify and characterize the functional proteins enriched in these EVs.

RESULTS

Cohousing with healthy mice prevents ONFH in the GC-treated cage mates

As mice eat each other's feces, they may transfer GM to their cage mates through feces, thus resulting in a transfer of some phenotypes to one another (*24*–*26*). To determine whether the exchange of GM can affect bone homeostasis in the mouse femoral head, we cohoused the mice receiving methylprednisolone (MPS) on the first 3 days of each week for 3 weeks with age-matched control mice treated with dimethyl sulfoxide (DMSO; the vehicle of MPS) using the same administration regimen (Fig. 1A). Micro–computed tomography (μCT) analysis showed that treatment with MPS caused large low-density area (osteonecrotic lesion) and remarkable bone loss in the femoral heads of mice, as indicated by the μCT-reconstructed images of femoral heads; the markedly decreased trabecular bone volume fraction (Tb. BV/TV), trabecular thickness (Tb. Th), and trabecular number (Tb. N); and the notably increased trabecular separation (Tb. Sp) in the MPS-treated mice compared with the vehicle-treated control mice (Fig. 1, B to F). Cohousing of the MPS-treated ONFH mice with the vehicle-treated normal mice resulted in significant improvement in trabecular bone microarchitecture in the femoral heads (Fig. 1, B to F), suggesting an environmental influence. As cohousing can lead to the exchange of GM components between cage mates via coprophagy (*24*–*26*), we hypothesized that cohousing might result in the transfer of microbes beneficial to bone health from healthy control mice to the MPS-treated mice. Unexpectedly, cohousing with MPS-treated mice did not induce ONFH phenotypes in the vehicle-treated cage mates, as revealed by the μCT-reconstructed images of femoral heads and the comparable levels of Tb. BV/TV, Tb. Th, Tb. N, and Tb. Sp in the cohoused and non-cohoused vehicle-treated mice (Fig. 1, B to F).

Hematoxylin and eosin (H&E) staining showed that the trabecular bone and marrow structures were profoundly destroyed or even completely eliminated in the femoral heads of most of the MPS-treated mice (Fig. 1G). Instead, the femoral heads were filled with fat vacuoles and degenerating cells with pyknotic nuclei and clear cytoplasm after MPS treatment (Fig. 1G), similar to that in the MPS-treated rats (*1*). Empty osteocytic lacunae (a sign of osteonecrosis) were detected in the residual trabecular bones of the femoral heads of MPS-treated mice but were rarely observed in those treated with vehicle only (Fig. 1G). The MPS-treated mice cohoused with vehicle-treated control mice showed much milder trabecular bone and marrow damage and lower numbers of empty osteocytic lacunae in the femoral heads, compared with the non-cohoused MPS-treated mice (Fig. 1G). However, no detrimental histological changes occurred in the femoral heads of the vehicle-treated mice cohoused with the MPS-treated mice (Fig. 1G).

μCT-based microangiography and immunohistochemical staining for the endothelial cell marker protein CD31 revealed that cohousing with the vehicle-treated age-matched control mice significantly rescued the MPS-induced reduction of blood vessels in the femoral heads, as indicated by the μCT-reconstructed images of blood vessels (Fig. 1H), the much higher vessel volume value (Fig. 1I), and the greater number of CD31-stained endothelial cells (Fig. 1, J and K). Immunostaining for osteocalcin [OCN; a marker of osteogenic activity (*27*)] showed a significant loss of OCN-positive osteoblasts in the mouse femoral head after MPS injection, while the decrease in osteoblast number was not so notable when the MPS-treated mice were cohoused with the vehicle-treated control mice (Fig. 1, L and M). Terminal deoxynucleotidyl transferase–mediated deoxyuridine triphosphate nick end labeling (TUNEL) staining showed that MPS caused remarkably increased cell apoptosis within the bone and bone marrow in the femoral heads of mice, but the effect was notably inhibited by cohousing with the vehicle-treated control mice (Fig. 1, N and O). However, cohousing with MPS-treated mice did not transfer their phenotypes, including blood vessel loss, osteogenesis impairment, and increased cell apoptosis, to vehicle-treated cage mates (Fig. 1, H to O). Enzyme-linked immunosorbent assay (ELISA) for a class of pro- or anti-inflammatory factors revealed that treatment with MPS only significantly reduced the serum level of the proinflammatory factor interleukin-1β (IL-1β) in the non-cohoused mice but did not result in remarkable changes of other inflammatory factors in the cohoused or non-cohoused mice (fig. S1, A to H), indicating that ONFH after GC administration with our protocol is not mainly associated with dysregulation of inflammation factor production. Cohousing with vehicle-treated healthy mice only induced a reduction of the proinflammatory factor IL-2 in the MPS-treated mice but just by trend (fig. S1, A to H). Together, the above findings suggest that the protective effects of cohousing with healthy mice on femoral heads are associated with the stimulation of angiogenic and osteogenic responses and/or the prevention of GC-induced apoptotic cell death but are not due to the modulation of inflammation.

Colonization with GM from normal mice attenuates GC-induced ONFH

We next investigated whether direct colonization of the conventionally raised GC-treated specific pathogen–free mice with GM from healthy mice by oral administration once a week for 6 weeks could trigger similar beneficial effects on femoral heads (Fig. 2A). As expected, μCT images of the femoral heads and trabecular bone microarchitecture parameters revealed that trabecular bone destruction induced by MPS was significantly reversed by transplantation with GM from the vehicle [phosphate-buffered solution (PBS)]–treated healthy mice (Fig. 2, B to F). Colonization with GM from the MPS-treated ONFH mice reduced Tb. BV/TV, Tb. Th, and Tb. N in the femoral heads of healthy mice but just by trend (Fig. 2, B to F). H&E staining determined that the MPS-treated mice had much larger areas of normal trabecular bone and marrow structures with fewer empty osteocytic lacunae in the femoral heads after oral gavage of GM from healthy mice (Fig. 2G). The MPS-treated mice transplanted with GM from the vehicle-treated healthy mice

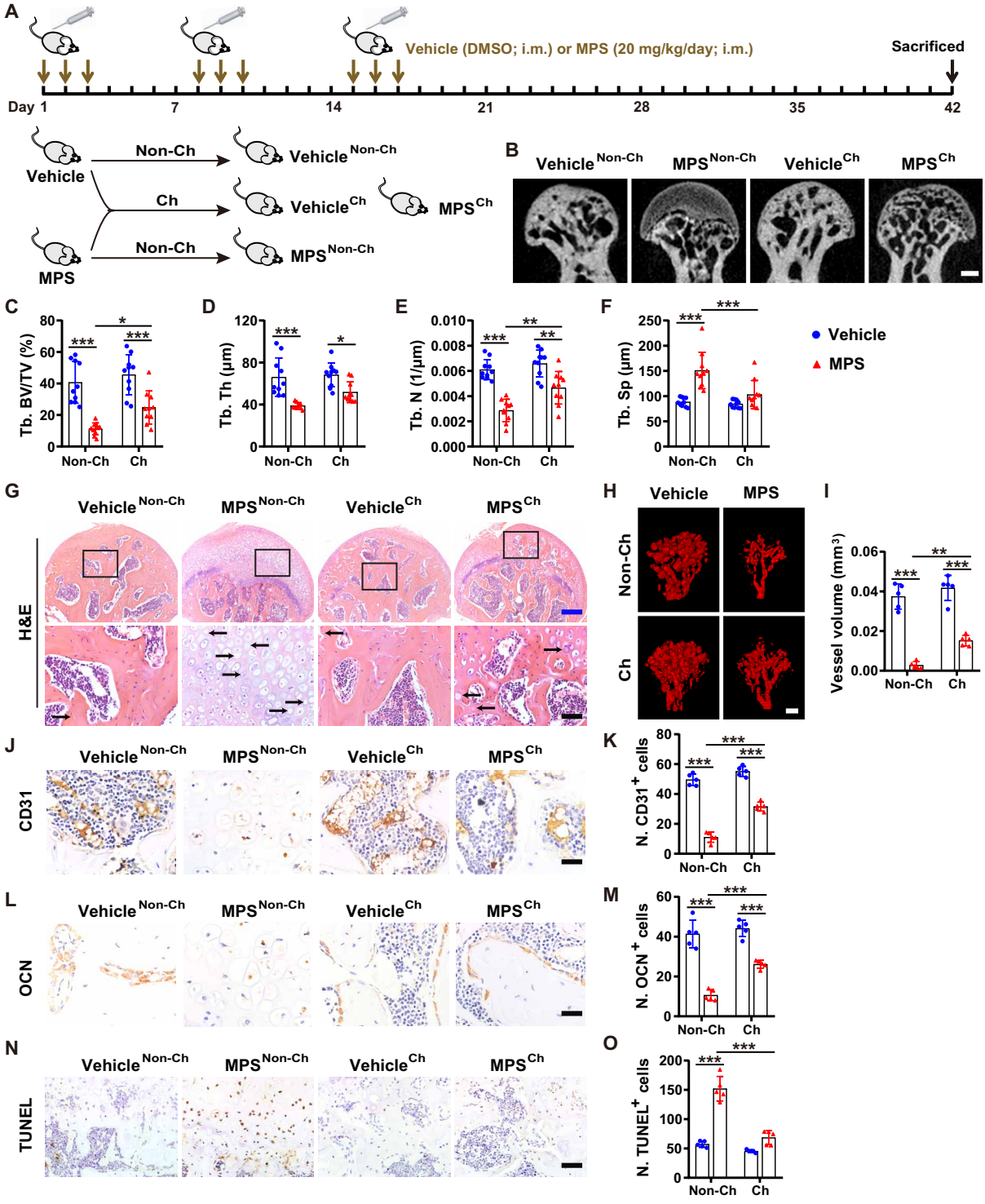

Fig. 1. Cohousing with healthy mice prevents ONFH in GC-treated cage mates. (**A**) Schematic diagram of the experimental design for assessing the effects of cohousing with the healthy or MPS-treated mice on the femoral heads of their cage mates. (**B** to **F**) μCT-reconstructed images (B) and quantification of Tb. BV/TV (C), Tb. Th (D), Tb. N (E), and Tb. Sp (F). Scale bar, 1 mm. $n = 10$ per group. (**G**) H&E staining images of femoral heads. The arrows indicate empty osteocytic lacunae. Scale bars, 200 μm (blue) or 50 μm (black). (**H**) Blood vessels in femoral heads visualized by μCT-based microangiography. Scale bar, 500 μm. (**I**) Quantification of total vessel volume. $n = 5$ per group. (**J**) CD31 immunostaining images of femoral heads. Scale bar, 25 μm. (**K**) Quantification of the number of $CD31^+$ cells. $n = 5$ per group. (**L**) Osteocalcin (OCN) immunostaining images of femoral heads. Scale bar, 25 μm. (**M**) Quantification of the number of OCN^+ cells. $n = 5$ per group. (**N**) Terminal deoxynucleotidyl transferase–mediated deoxyuridine triphosphate nick end labeling (TUNEL) staining images of femoral heads. Scale bar, 50 μm. (**O**) Quantification of the number of $TUNEL^+$ cells. $n = 5$ per group. $^*P < 0.05$, $^{**}P < 0.01$, and $^{***}P < 0.001$. i.m., intramuscularly.

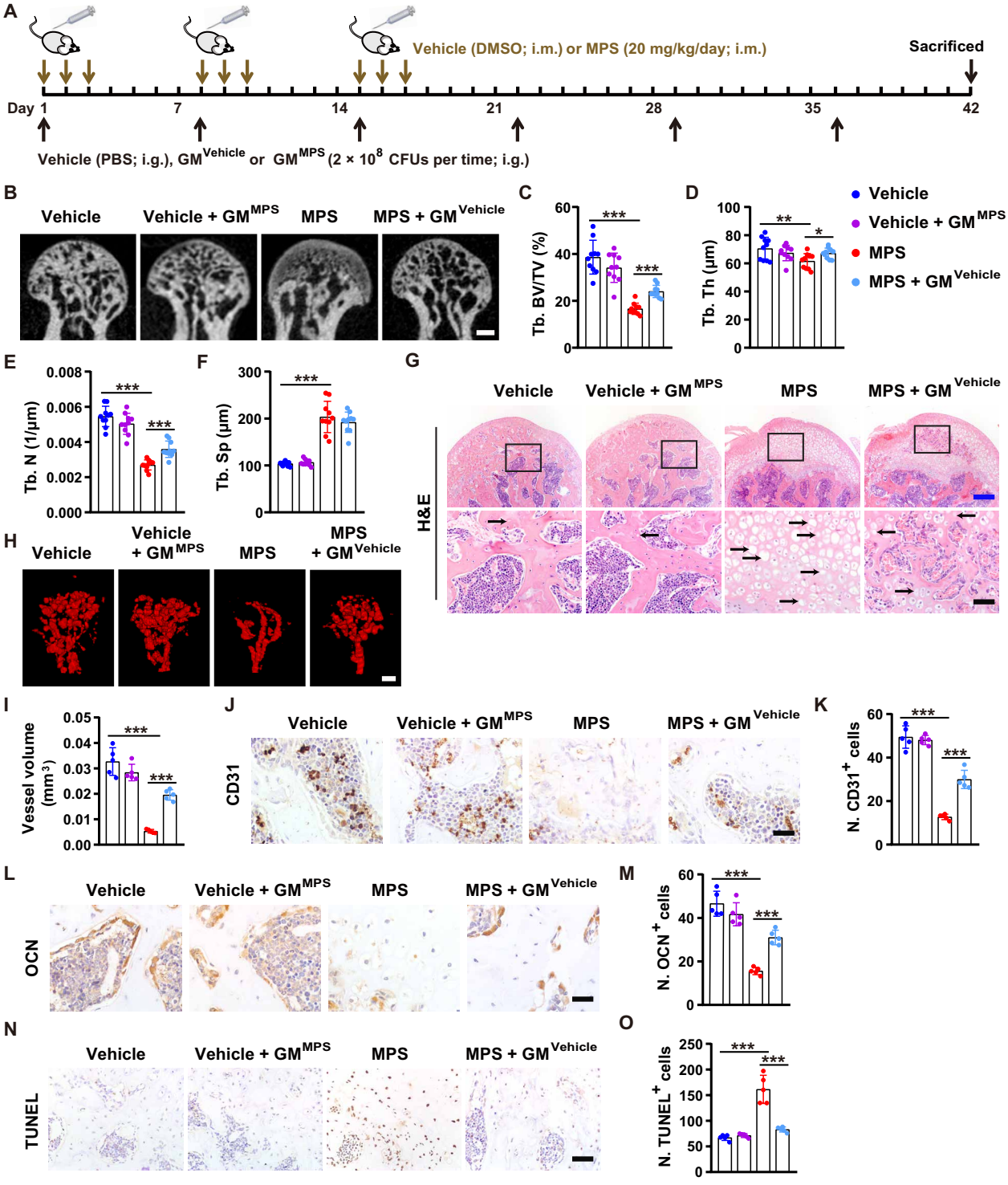

Fig. 2. Colonization with GM from normal mice attenuates GC-induced ONFH. (**A**) Schematic diagram of the experimental design for exploring the effects of oral treatment with GM from MPS-treated mice (GM^{MPS}) or vehicle-treated healthy mice ($GM^{Vehicle}$) on the femoral heads of the vehicle- or MPS-treated mice. (**B** to **F**) μCT-reconstructed images of femoral heads (B) and quantification of Tb. BV/TV (C), Tb. Th (D), Tb. N (E), and Tb. Sp (F). Scale bar, 1 mm. $n = 10$ per group. (**G**) H&E staining images of femoral heads. Scale bars, 200 μm (blue) or 50 μm (black). (**H**) μCT-reconstructed images of the Microfil-perfused blood vessels in femoral heads. Scale bar, 500 μm. (**I**) Quantification of total vessel volume. $n = 5$ per group. (**J**) CD31 immunostaining images of femoral heads. Scale bar, 25 μm. (**K**) Quantification of the number of $CD31^+$ cells. $n = 5$ per group. (**L**) OCN immunostaining images of femoral heads. Scale bar, 25 μm. (**M**) Quantification of the number of OCN^+ cells. $n = 5$ per group. (**N**) TUNEL staining images of femoral heads. Scale bar, 50 μm. (**O**) Quantification of the number of $TUNEL^+$ cells. $n = 5$ per group. $^*P < 0.05$, $^{**}P < 0.01$, and $^{***}P < 0.001$. i.g., intragastric

exhibited markedly increased blood vessels and OCN-positive osteoblasts, as well as significantly decreased apoptotic cells in the femoral heads, compared with the nontransplanted MPS-treated mice, as shown by the blood vessel images visualized by μCT-based microangiography (Fig. 2H), quantitative data of blood vessel volume (Fig. 2I), immunostaining for CD31 (Fig. 2, J and K) and OCN (Fig. 2, L and M), and TUNEL staining of apoptotic cells (Fig. 2, N and O), respectively. Consistent with that observed in the healthy control mice cohoused with MPS-treated mice, the direct transplantation of the healthy mice with GM from MPS-treated mice had no obvious deleterious effects on trabecular bone and bone marrow structures (Fig. 2G); moreover, this treatment did not induce remarkable changes in blood vessel density (Fig. 2, H to K), osteoblast abundance (Fig. 2, L and M), and apoptotic cell number (Fig. 2, N and O) in the femoral heads of the healthy mice. ELISA showed that GM from the vehicle- or MPS-treated mice did not induce statistically significant changes in the serum levels of many proinflammatory [IL-1α, IL-1β, IL-2, IL-6, IL-8, tumor necrosis factor–α (TNF-α), and interferon-γ (IFN-γ)] and anti-inflammatory (IL-4) factors in the MPS- or vehicle-treated mice (fig. S2, A to H).

To exclude the influence of the endogenous GM in the mice, we then obtained microbiota-depleted mice by treatment of the specific pathogen–free mice with a cocktail of broad-spectrum antibiotics as described previously (*28*) and tested the impact of GM from the vehicle-treated healthy mice or the MPS-treated ONFH mice on trabecular bone microarchitecture in the femoral heads of the microbiota-depleted mice receiving vehicle or MPS treatment. μCT analysis revealed that MPS treatment resulted in significant trabecular bone damage and bone loss in the femoral heads of the microbiota-depleted mice (fig. S3, A to E), indicating that GC can damage femoral head through a GM-independent mechanism. Transplantation with GM from the vehicle-treated healthy mice significantly reversed the MPS-induced reductions of Tb. BV/TV, Tb. Th, and Tb. N in the microbiota-depleted MPS-treated mice, consistent with that observed in the conventionally raised MPS-treated mice. Colonization with GM from the MPS-treated mice not only caused a marked reduction of Tb. BV/TV in the microbiota-depleted vehicle-treated mice but also resulted in a significant decrease in Tb. N and a remarkable increase in Tb. Sp in the microbiota-depleted MPS-treated mice, indicating that transplantation with GM from MPS-treated mice can induce harmful effects on femoral heads in the microbiota-depleted control mice and exacerbate ONFH phenotype in the microbiota-depleted MPS-treated mice (fig. S3, A to E).

Collectively, these findings suggest that GM from the healthy mice contains microbe that can protect against GC-induced ONFH by promoting angiogenesis, enhancing osteogenesis, and/or inhibiting cell apoptosis. In the GC-treated mice, there seem to exist gut microbes that have detrimental effects on femoral head, but transplantation with GM from these mice at our current regimen is not sufficient to transfer the ONFH phenotypes to the conventionally raised healthy mice after colonization.

Cohousing with healthy mice rescues the loss of *Lactobacillus animalis* induced by GC

To explore the microbe that mediates the protective effects of GM from the healthy mice against GC-induced ONFH, we harvested fecal samples from the MPS- or vehicle-treated male mice cohoused with or without the age-matched male mice receiving vehicle or MPS treatment at the first 3 days in a week for 3 weeks. 16*S* rRNA gene sequencing was conducted to assess the changes of gut microbes in these mice. Figure 3A shows that MPS treatment resulted in a trend of decrease in the observed number of operational taxonomic units (OTUs) and estimated OTU richness [Chao1 and abundance-based coverage estimator (ACE)] in fecal microbiota, but the reduction of community richness was reversed in the MPS-treated mice cohoused with vehicle-treated control mice. The microbial community composition, relative abundance, and absolute copy numbers of the identified fecal microbiota at the phylum, class, order, family, genus, and species levels are shown in Fig. 3B and tables S1 and S2. The results revealed that cohousing with the vehicle-treated healthy control mice or MPS-treated mice caused an increase in the absolute abundance of the total fecal bacteria in most of their cage mates (Fig. 3B and tables S1 and S2), suggesting that cohousing-mediated GM transfer alters total microbial abundance in both the cohoused control mice and MPS-treated mice. At the genus level, treatment with MPS led to a reduction in the relative and absolute abundance of *Lactobacillus* compared with vehicle-treated control mice, but the loss of *Lactobacillus* absolute abundance induced by MPS was significantly rescued by cohousing with the vehicle-treated control mice (Fig. 3, B and C, and tables S1 and S2), suggesting that cohousing may result in transfer of bacteria in the genus *Lactobacillus* from the healthy control mice to MPS-treated cage mates. At the species level, *L. animalis* and *Lactobacillus intestinalis* were reduced in the fecal microbiota of MPS-treated mice compared to vehicle-treated controls (Fig. 3D and tables S1 and S2). However, the relative and absolute abundance of *L. animalis* was increased only in some of the cohoused MPS-treated mice compared with non-cohoused MPS-treated mice and comparable in the cohoused and non-cohoused vehicle-treated mice (Fig. 3D and tables S1 and S2). We then collected feces from the mice treated with vehicle or MPS on the first 3 days of each week for 1, 2, and 3 weeks and used quantitative real-time polymerase chain reaction (qRT-PCR) to compare *L. animalis* abundance in fecal microbiota between the vehicle- and MPS-treated mice. The results showed that MPS induced a significant reduction in *L. animalis* abundance at 1 week after administration, and *L. animalis* was maintained at a very low level at 2 and 3 weeks after treatment (Fig. 3E), which further suggests the inhibition of growth and/or survival of *L. animalis* after GC administration. These results suggest that *L. animalis* may be the key beneficial microbe that mediates the bone-protective effects of GM from healthy mice against GC-induced ONFH.

Transplantation with *L. animalis* protects against GC-induced ONFH

We then determined whether transplantation of *L. animalis* by oral gavage once a week for 6 weeks was able to protect mice from GC-induced ONFH (Fig. 3F). μCT analysis revealed that oral administration of *L. animalis* markedly attenuated MPS-induced trabecular bone damage, decreases in Tb. BV/TV and Tb. N, and increase in Tb. Sp (Fig. 3, G to K). In healthy mice, treatment with *L. animalis* also significantly enhanced Tb. BV/TV and induced a trend of increases in Tb. Th and Tb. N, as well as a decrease in Tb. Sp (Fig. 3, G to K), indicating that *L. animalis* can not only exert bone-protective effects in the GC-induced ONFH mice but also benefit bone in healthy mice. Consistently, H&E staining showed that the MPS + *L. animalis*–treated mice exhibited much milder trabecular bone and marrow destruction in the femoral heads compared with the mice receiving MPS only (Fig. 3L). Transplantation

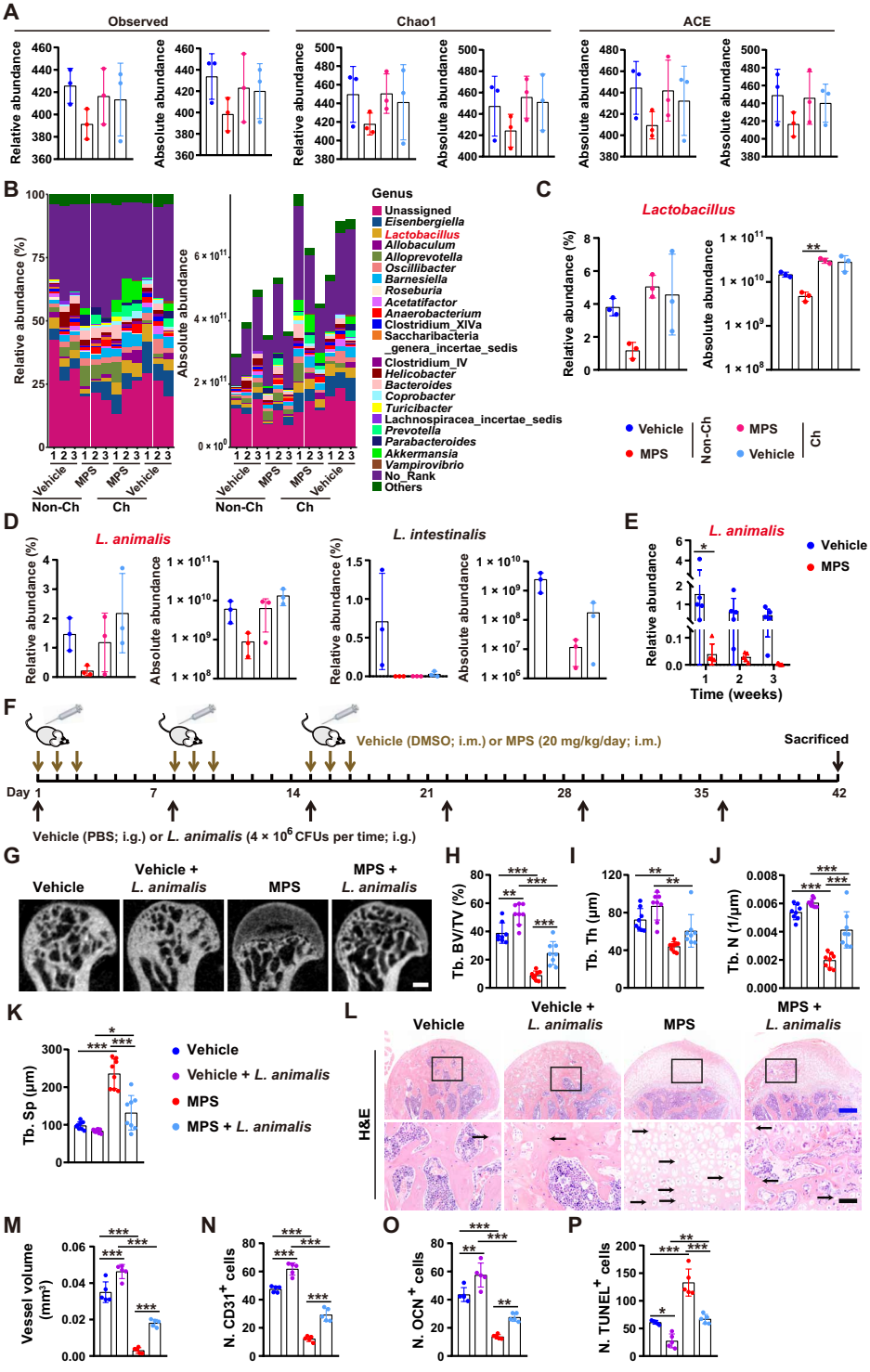

Fig. 3. Cohousing with healthy mice rescues the GC-induced loss of *L. animalis*, and transplantation with *L. animalis* protects against GC-induced ONFH. (**A**) Observed number of OTUs and estimated OTU richness (Chao1 and ACE) in fecal microbiota from the cohoused (Ch) or non-cohoused (Non-Ch) vehicle- or MPS-treated mice. $n = 3$ per group. (**B**) Relative and absolute abundance of the identified fecal microbiota at the genus level tested by 16*S* rRNA gene sequencing. $n = 3$ per group. (**C** and **D**) Relative and absolute abundance of the genus *Lactobacillus* (C) and the species *L. animalis* and *L. intestinalis* (D) in fecal microbiota from mice in (A). $n = 3$ per group. (**E**) qRT-PCR analysis of *L. animalis* abundance in fecal microbiota from mice receiving vehicle or MPS for 1, 2, and 3 weeks. $n = 5$ per group. (**F**) Schematic diagram of the experimental design for testing the effects of oral treatment with *L. animalis* on the femoral heads of vehicle- or MPS-treated mice. (**G** to **K**) μCT-reconstructed images of femoral heads (G) and quantification of Tb. BV/TV (H), Tb. Th (I), Tb. N (J), and Tb. Sp (K). Scale bar, 1 mm. $n = 8$ per group. (**L**) H&E staining images of femoral heads. Scale bars, 200 μm (blue) or 50 μm (black). (**M** to **P**) Quantification of total vessel volume (M) and the numbers of $CD31^+$ (N), OCN^+ (O), and $TUNEL^+$ (P) cells in femoral heads. $n = 5$ per group. $^*P < 0.05$, $^{**}P < 0.01$, and $^{***}P < 0.001$.

with *L. animalis* also markedly rescued the reduction of blood vessels and osteoblast abundance and significantly suppressed cell apoptosis in the femoral heads of the MPS-treated mice, as evidenced by the much higher value of blood vessel volume (Fig. 3M), higher numbers of CD31- and OCN-positive cells (Fig. 3, N and O), and lower number of TUNEL-stained apoptotic cells (Fig. 3P) in the femoral heads of the MPS + *L. animalis*–treated mice compared to MPS-treated mice. After oral gavage of *L. animalis*, the healthy mice also showed notably higher abundance of blood vessels and osteoblasts and lower number of apoptotic cells in the femoral heads compared with the vehicle-treated control mice (Fig. 3, M to P). No statistically significant changes in serum levels of inflammatory factors were induced in the vehicle- and MPS-treated mice receiving *L. animalis* transplantation (fig. S4, A to H). These findings indicate that *L. animalis* can promote vascularization, augment osteogenesis, suppress cell apoptosis, and improve trabecular bone microarchitecture in the femoral head under either normal or GC-induced osteonecrotic condition.

Direct effects of EVs from *L. animalis* on angiogenesis, osteogenesis, and apoptosis

We next isolated EVs from the culture medium (CM) of *L. animalis* and investigated the direct effects of these EVs (*L. animalis*-EVs) on angiogenesis, osteogenesis, and apoptosis. *L. animalis*-EVs displayed cup-like morphologies with diameters of 118.8 ± 49.5 nm, as shown by transmission electron microscopy (Fig. 4A) and diameter analysis by nanoparticle tracking analysis (Fig. 4B). Nanoparticle tracking analysis also showed that the vesicle numbers in 100 μg of *L. animalis*-EVs from different batches were at the range of (3.7 to 4.6) × 10^{10} vesicles (Fig. 4C). *L. animalis*-EVs were labeled with a lipophilic dye DiO (green) or DiI (red) and incubated with human microvascular endothelial cells (HMECs), mouse long bone osteocyte-Y4 (MLO-Y4), mouse preosteoblast MC3T3-E1 cells, and mouse bone marrow mesenchymal stem cells (BMSCs) for 3 hours. As shown in Fig. 4D, the DiO- or DiI-labeled *L. animalis*-EVs could be taken up by these cells and accumulated in the perinuclear region, suggesting that *L. animalis*-EVs may be able to directly modulate their function.

Tube formation assay showed that MPS significantly impaired the ability of HMECs to form capillary-like network structures on Matrigel, as shown by the images of HMECs under an optical microscope and the much lower values of total loops and total tube length in the MPS-treated cells compared with vehicle-treated control cells (Fig. 4, E to G). Unexpectedly, cotreating with *L. animalis*-EVs resulted in a dose-dependent increase in tube formation of the MPS-treated HMECs at the dose of 2.5 to 10 μg/ml (Fig. 4, E to G). Although *L. animalis*-EVs at the concentration of 20 μg/ml also blocked the MPS-induced inhibitory effect on angiogenic activity of HMECs, the effect was much lower than that of *L. animalis*-EVs at the dose of 10 μg/ml (Fig. 4, E to G). Thus, we selected the dose of 10 μg/ml for the downstream *L. animalis*-EV–related experiments in vitro. Besides, in the MPS-treated endothelial cells, *L. animalis*-EVs also exhibited a profound proangiogenic effect in the vehicle-treated normal endothelial cells, as shown by the tube formation images of HMECs (Fig. 4H) and the significantly increased values of total loops and total tube length compared with the vehicle-treated control cells (Fig. 4, I and J). We also compared the proangiogenic effect of *L. animalis*-EVs with EVs from *Lactobacillus reuteri* ATCC PTA 6475 (a probiotic bacterium that resides in the human gut). Tube formation assay revealed that *L. reuteri*–derived EVs (*L. reuteri*-EVs) also significantly increased the ability of HMECs to form tubes in both the vehicle- and MPS-treated groups, but the positive effect of *L. reuteri*-EVs on tube formation was much lower than that of *L. animalis*-EVs (Fig. 4, H to J).

Alizarin red S (ARS) staining indicated that MPS treatment resulted in a significant inhibition of mineralized nodule formation of BMSCs under osteogenic differentiation (Fig. 4, K and L). Incubation with *L. animalis*-EVs not only remarkably blocked the MPS-induced negative effect on osteogenic differentiation of BMSCs but also induced a further increase in BMSC mineralization in the vehicle-treated normal group (Fig. 4, K and L), indicating that *L. animalis*-EVs can directly stimulate BMSC osteogenesis. However, treatment with *L. reuteri*-EVs just slightly increased mineralized nodule formation in BMSCs treated with or without MPS under osteogenic induction, indicating that *L. reuteri*-EVs have no significant direct positive effect on osteogenesis of BMSCs (Fig. 4, K and L).

Cell counting kit-8 (CCK-8) assay showed that cotreatment with *L. animalis*-EVs or *L. reuteri*-EVs profoundly blocked the MPS-induced reduction of survival/growth of HMECs, MLO-Y4, MC3T3-E1, and BMSCs (Fig. 4, M to P). The protective effects of *L. animalis*-EVs against HMECs, MLO-Y4, and MC3T3-E1 were comparable to or slightly higher or lower than that of *L. reuteri*-EVs (Fig. 4, M to O). In the MPS-treated BMSCs, the positive effect of *L. animalis*-EVs on cell survival/growth was significantly higher than that of *L. reuteri*-EVs (Fig. 4P). TUNEL staining indicated that both *L. animalis*-EVs and *L. reuteri*-EVs could markedly attenuate the MPS-induced apoptosis of these cells (Fig. 4, Q and R), suggesting that the direct inhibition of apoptosis contributes to their protective effects against GC-induced cell death. In the MPS-treated MLO-Y4 and BMSCs, the antiapoptotic effect of *L. animalis*-EVs was much higher than that of *L. reuteri*-EVs (Fig. 4, Q and R).

We also performed tube formation assay to assess whether *L. animalis*-EVs could indirectly regulate the angiogenic activity of endothelial cells by stimulating cells to secrete proangiogenic factors. The CMs of the vehicle- or *L. animalis*-EV–pretreated HMECs, MLO-Y4, MC3T3-E1, and BMSCs were harvested, and their effects on tube formation of endothelial cells were assessed. The results showed that incubation with the CMs from the vehicle-pretreated HMECs ($HMECs^{Vehicle}$-CM), MLO-Y4 ($MLO\text{-}Y4^{Vehicle}$-CM), MC3T3-E1 ($MC3T3\text{-}E1^{Vehicle}$-CM), and BMSCs ($BMSCs^{Vehicle}$-CM) induced a statistically significant increase in the ability of HMECs to form tubes on Matrigel, as compared with the cells treated with the uncultured control medium (fig. S5, A to L). When HMECs were treated with the CMs from the *L. animalis*-EV–pretreated HMECs ($HMECs^{L\text{-}EVs}$-CM) and MLO-Y4 ($MLO\text{-}Y4^{L\text{-}EVs}$-CM), much more vascular tube-like structures were formed, as revealed by the images of HMECs and the much higher values of total loops and total tube length compared with the cells treated with $HMECs^{Vehicle}$-CM and $MLO\text{-}Y4^{Vehicle}$-CM, respectively (fig. S5, A to F). Pretreatment of MC3T3-E1 and BMSCs with *L. animalis*-EVs had no significant effects on their ability to augment angiogenic tube formation of HMECs (fig. S5, G to L).

Together, the above results indicate that *L. animalis*-EVs can enter endothelial cells and bone cells to directly enhance endothelial angiogenesis, augment BMSC osteogenesis, and prevent GC-induced apoptotic cell death. Furthermore, *L. animalis*-EVs can also stimulate endothelial cells and osteocytes to secrete proangiogenic factors.

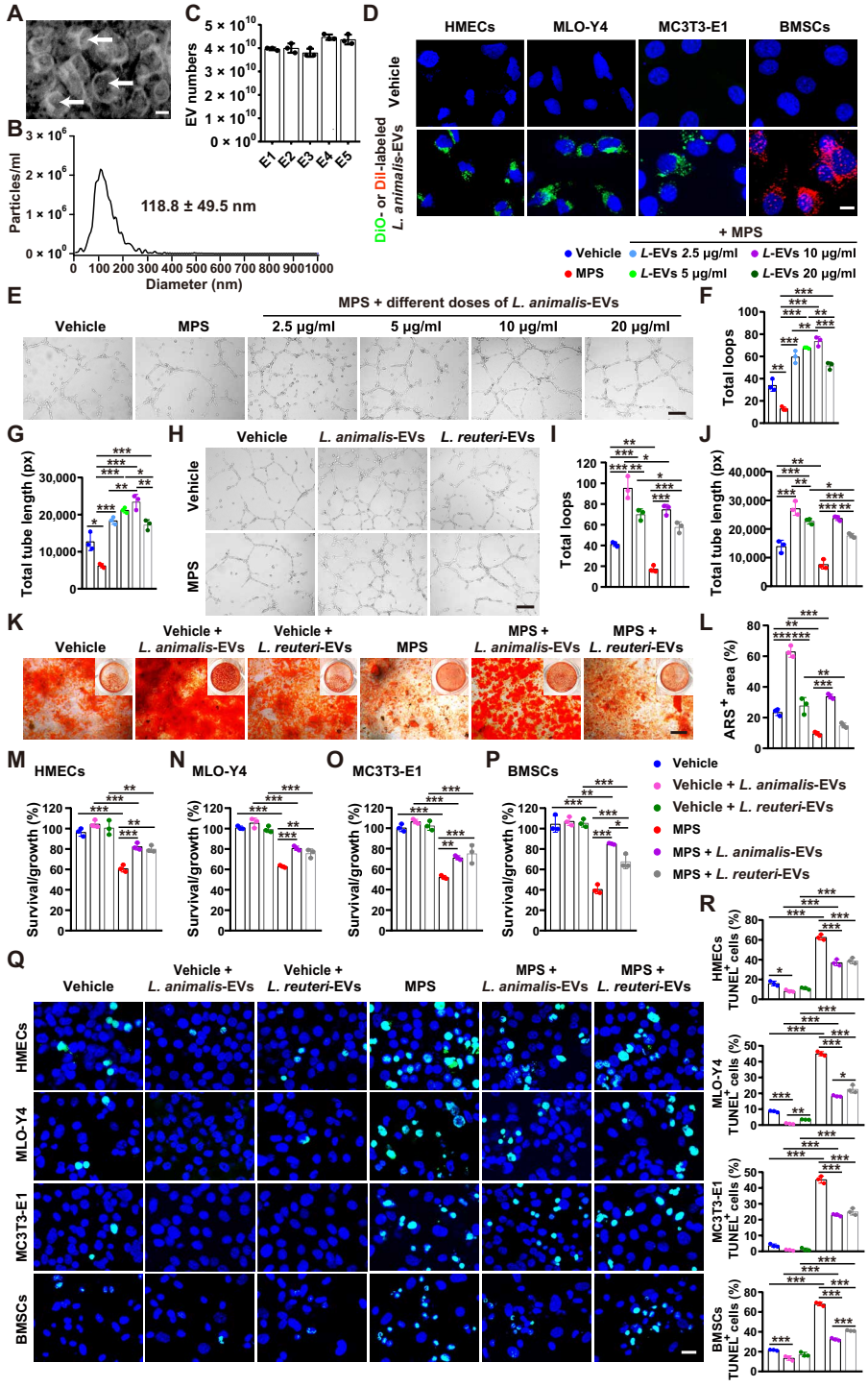

Fig. 4. *L. animalis*-EVs directly promote angiogenesis, augment osteogenesis, and reduce cell apoptosis. (**A**) Morphology of *L. animalis*-EVs under a transmission electron microscope. Scale bar, 50 nm. (**B**) Diameter measurement of *L. animalis*-EVs by nanoparticle tracking analysis. (**C**) Quantification of vesicle numbers in 100 μg of *L. animalis*-EVs from five different batches (E1, E2, E3, E4, and E5) by nanoparticle tracking analysis. $n = 3$ per group. (**D**) Uptake of the DiO (green)– or DiI (red)–labeled *L. animalis*-EVs by HMECs, MLO-Y4, mouse preosteoblast MC3T3-E1 cells, and BMSCs. Scale bar, 10 μm. (**E**) Tube formation images of HMECs treated with vehicle, MPS, or MPS + different concentrations of *L. animalis*-EVs (*L*-EVs). Scale bar, 200 μm. (**F** and **G**) Quantification of total loops (F) and total tube length (G). $n = 3$ per group. (**H**) Tube formation images of HMECs treated with vehicle, vehicle + *L. animalis*-EVs, vehicle + *L. reuteri*-EVs, MPS, MPS + *L. animalis*-EVs, or MPS + *L. reuteri*-EVs. Scale bar, 200 μm. (**I** and **J**) Quantification of total loops (I) and total tube length (J). $n = 3$ per group. (**K**) Alizarin red S (ARS) staining images of BMSCs with different treatments under osteogenic induction. Scale bar, 200 μm. (**L**) Quantification of the percentage of ARS^+ areas. $n = 3$ per group. (**M** to **P**) Cell counting kit-8 (CCK-8) analysis of HMECs (M), MLO-Y4 (N), MC3T3-E1 (O), and BMSCs (P) with different treatments. $n = 3$ per group. (**Q** and **R**) TUNEL staining images of different cell types receiving different treatments (Q) and quantification of the ratio of $TUNEL^+$ apoptotic cells (R). Scale bar, 20 μm. $n = 3$ per group. $^*P < 0.05$, $^{**}P < 0.01$, and $^{***}P < 0.001$.

L. animalis-EVs enter the femoral head and mitigate GC-induced ONFH

To explore whether the administration of *L. animalis*-EVs can induce bone benefits in GC-induced ONFH mice, we first assessed whether these bacterial EVs could be transported to the femoral heads of GC-treated mice after intragastric administration. Ex vivo fluorescent imaging showed the presence of fluorescent signals in many tissues from the mice orally treated with the DiR iodide–labeled *L. animalis*-EVs for 3 hours by oral route, among which the liver, spleen, lungs, gastrointestine, kidneys, and bones displayed much higher fluorescence intensity compared with other tissues (Fig. 5, A and B, and fig. S6, A and B), suggesting that *L. animalis*-EVs are mainly accumulated in these sites after oral administration. The femoral heads displayed a large area of red fluorescent signals at 3 hours after administration (Fig. 5, A and B), indicating that a vast number of *L. animalis*-EVs can enter the femoral head. After administration for 24 hours, fluorescence intensity in the majority of the above-described tissues with high levels of *L. animalis*-EV accumulation was significantly decreased (Fig. 5, A and B, and fig. S6, A and B). After 72 hours of treatment, most of the tissues showed low fluorescence intensity in the mice orally treated with the DiR-labeled *L. animalis*-EVs (Fig. 5, A and B, and fig. S6, A and B), indicating that most of the *L. animalis*-EVs were metabolized and used by the recipient mice after administration for 72 hours. However, some fluorescence remained in most of the detected tissues (including the femoral heads) (Fig. 5, A and B, and fig. S6, A and B), indicating that *L. animalis*-EVs were not completely metabolized by the cells within these tissues at this time point. Uptake of *L. animalis*-EVs by cells within the femoral head was then confirmed by the presence of green fluorescent signals in trabecular bone and bone marrow of the femoral heads from the mice receiving the DiO-labeled *L. animalis*-EVs for 3 hours by oral gavage but not from the vehicle-treated mice (Fig. 5C). We also used *L. animalis*-EVs to immunize rabbits and obtained the serum containing the specific antibodies targeting *L. animalis*-EVs to further determine the presence and abundance of these EVs in the femoral heads of the vehicle- or MPS-treated mice orally administered with *L. animalis*-EVs or its vehicle (PBS) once a week for 3 weeks (Fig. 5D). As shown in Fig. 5 (E and F), a certain amount of fluorescence was observed in the femoral heads of the vehicle-treated control mice (Fig. 5, E and F). MPS treatment caused a significant loss of fluorescent signals in the femoral heads, but the fluorescence was markedly increased in the MPS-treated mice orally administered with *L. animalis*-EVs (Fig. 5, E and F), suggesting that *L. animalis*-EVs can be transported to the host femoral head under physiological conditions, and the exogenous administration of *L. animalis*-EVs by an oral route can rescue the MPS-induced reduction of these EVs.

We then determined whether the oral administration of *L. animalis*-EVs once a week for 6 weeks at the early stage of GC exposure was sufficient to attenuate GC-induced ONFH (Fig. 5D). As evidenced by μCT analysis, smaller low-density osteonecrotic area, higher Tb. BV/TV and Tb. N, and lower Tb. Sp were observed in the femoral heads of the MPS + *L. animalis*-EV–treated mice compared with the mice treated with MPS only (Fig. 5, G to K). Similar to their parent bacterium *L. animalis*, *L. animalis*-EVs also improved trabecular bone microarchitecture in healthy control mice, as indicated by significant increases in Tb. BV/TV and Tb. Th in the *L. animalis*-EV–treated mice relative to vehicle-treated mice (Fig. 5, G to K). H&E staining demonstrated that *L. animalis*-EVs reduced empty osteocytic lacunae and mitigated trabecular bone and marrow destruction in the MPS-treated mice (Fig. 5L). *L. animalis*-EVs also remarkably increased blood vessel volume (Fig. 5M), augmented the numbers of CD31-positive endothelial cells (Fig. 5N) and OCN-stained osteoblasts (Fig. 5O), and decreased apoptotic cell number (Fig. 5P) in the femoral heads of both MPS-treated mice and vehicle-treated healthy mice, as indicated by quantitative measurement of blood vessels using μCT-based microangiography, immunostaining for CD31 and OCN, and apoptotic cell staining by TUNEL, respectively. ELISA revealed that *L. animalis*-EV administration just resulted in a significant reduction in the serum level of TNF-α in the vehicle-treated healthy mice and a trend of decreases in the serum levels of IL-2 and IFN-γ in both vehicle- and MPS-treated mice (fig. S7, A to H). These findings suggest that *L. animalis*-EVs can improve bone microarchitecture and prevent GC-induced ONFH by enhancing blood vessel abundance, increasing osteogenic activity, and reducing cell apoptosis.

We next tested the effects of *L. animalis*-EVs and their parent bacterium *L. animalis* on trabecular bone microarchitecture in the femoral heads of mice in which GC-induced ONFH had been developed by MPS treatment for many times. μCT analysis revealed that both *L. animalis*-EVs and *L. animalis* could not notably reverse trabecular bone damage and bone loss in the femoral heads of mice in which ONFH had already been induced by MPS (fig. S8, A to E), indicating that treatment with *L. animalis*-EVs and *L. animalis* at the later stage of ONFH cannot induce obvious benefits on bone in the femoral head.

Proteomic analysis of *L. animalis*-EVs and *L. animalis*

Label-free proteomic analysis was applied to characterize and quantify proteins in *L. animalis*-EVs and their parent bacterium *L. animalis*. In total, there were 1136 proteins that were identified in *L. animalis*-EVs and/or *L. animalis*, among which 340 proteins were quantified (Fig. 6A). The differentially expressed proteins ($P < 0.05$; $|\text{fold change}| \geq 1.5$) between *L. animalis*-EVs and *L. animalis* are listed in table S3 and illustrated as a volcano plot in Fig. 6B. In total, 74 proteins were much higher and 140 proteins were much lower in *L. animalis*-EVs compared with *L. animalis* (Fig. 6B and table S3). The top 10 most abundant proteins in *L. animalis*-EVs relative to *L. animalis* are shown in Fig. 6C. Gene Ontology (GO) annotation was conducted to classify the proteins highly enriched in *L. animalis*-EVs relative to *L. animalis* according to their subcellular localizations. As shown in Fig. 6D, 25.68% of them were from cytoplasmic and 18.92% of them were annotated as cytoplasmic membrane proteins. The subcellular localizations of 47.30% proteins were unknown, and the remaining proteins were from cell wall (6.75%) or extracellular (1.35%) (Fig. 6D). GO biological process enrichment analysis of the up-regulated proteins revealed that *L. animalis*-EVs were enriched with proteins involved in the transport of neutral amino acid, organic acid transmembrane, L-amino acid, etc. (Fig. 6E), supporting the notion that EVs act as important cellular material transporters between cells. *L. animalis*-EVs were also enriched with proteins associated with nucleoside diphosphate phosphorylation, nucleotide phosphorylation, or nucleoside diphosphate metabolic process (Fig. 6E), suggesting a functional role of *L. animalis*-EVs in cell metabolism. Kyoto Encyclopedia of Genes and Genomes (KEGG) pathway enrichment analysis showed that the up-regulated proteins in *L. animalis*-EVs compared with *L. animalis* were involved in nucleotide-binding oligomerization

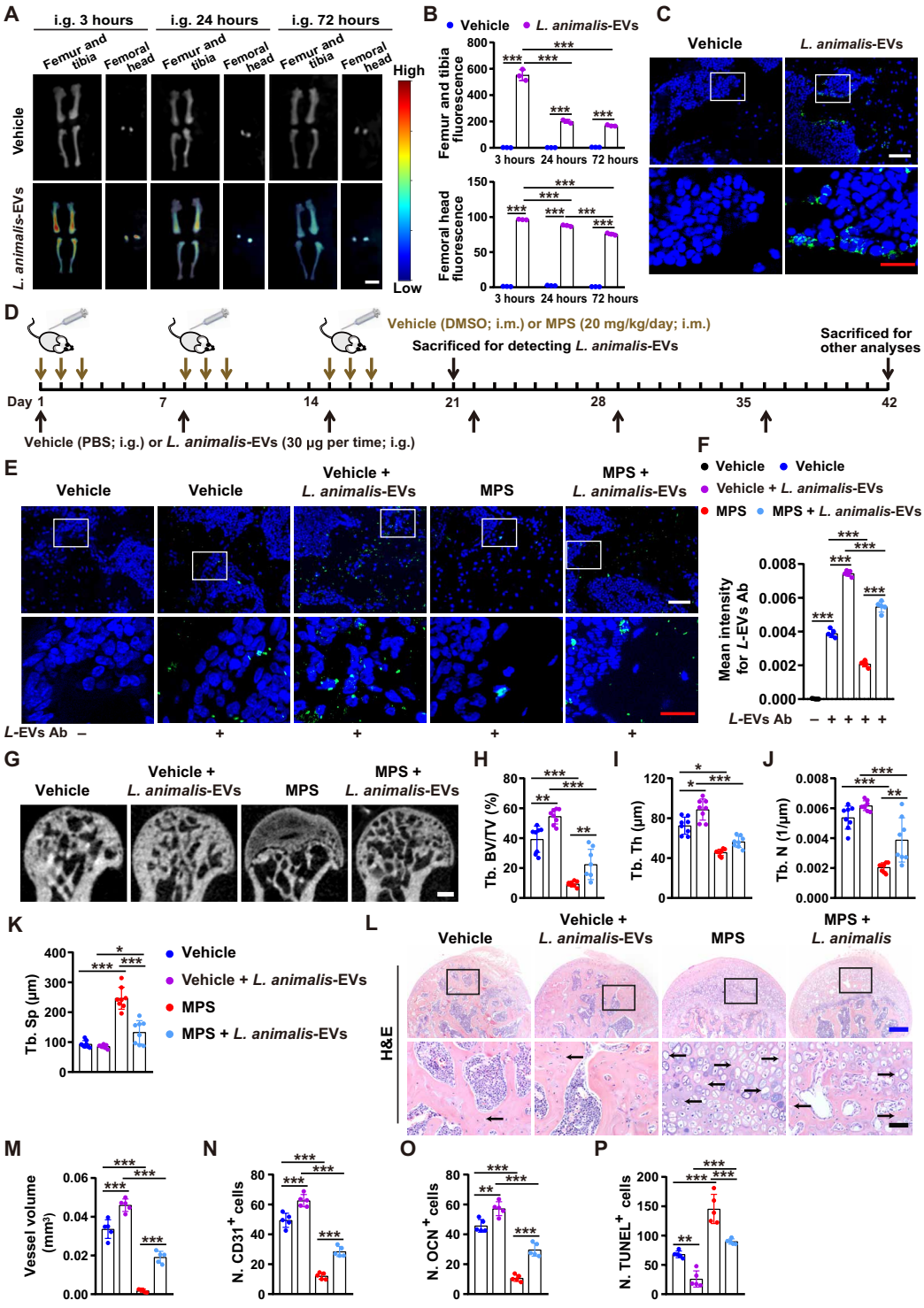

Fig. 5. *L. animalis*-EVs enter the femoral head and mitigate GC-induced ONFH. (**A**) Distribution of the DiR-labeled *L. animalis*-EVs in the femurs, tibias, and femoral heads of mice detected by ex vivo fluorescent imaging after oral administration for 3, 24, and 72 hours. Scale bar, 6 mm. (**B**) Quantification of the fluorescence intensity. $n = 3$ per group. (**C**) Distribution of the DiO-labeled *L. animalis*-EVs within the mouse femoral head after oral administration for 3 hours. Scale bars, 50 μm (white) or 20 μm (red). (**D**) Schematic diagram of the experimental design for testing the effects of oral treatment with *L. animalis*-EVs on the femoral heads of vehicle- or MPS-treated mice. (**E**) Detection of *L. animalis*-EVs in the mouse femoral heads using the antibodies targeting *L. animalis*-EVs (*L*-EVs Ab). Scale bars, 50 μm (white) or 20 μm (red). (**F**) Quantification of the mean intensity for *L*-EV$^+$ areas. $n = 3$ per group. (**G** to **K**) μCT-reconstructed images of femoral heads (G) and quantification of Tb. BV/TV (H), Tb. Th (I), Tb. N (J), and Tb. Sp (K). Scale bar, 1 mm. $n = 8$ per group. (**L**) H&E staining images of femoral heads. Scale bars, 200 μm (blue) or 50 μm (black). (**M** to **P**) Quantification of total vessel volume (M) and the numbers of CD31$^+$ (N), OCN$^+$ (O), and TUNEL$^+$ (P) cells in femoral heads. $n = 5$ per group. $^*P < 0.05$, $^{**}P < 0.01$, and $^{***}P < 0.001$.

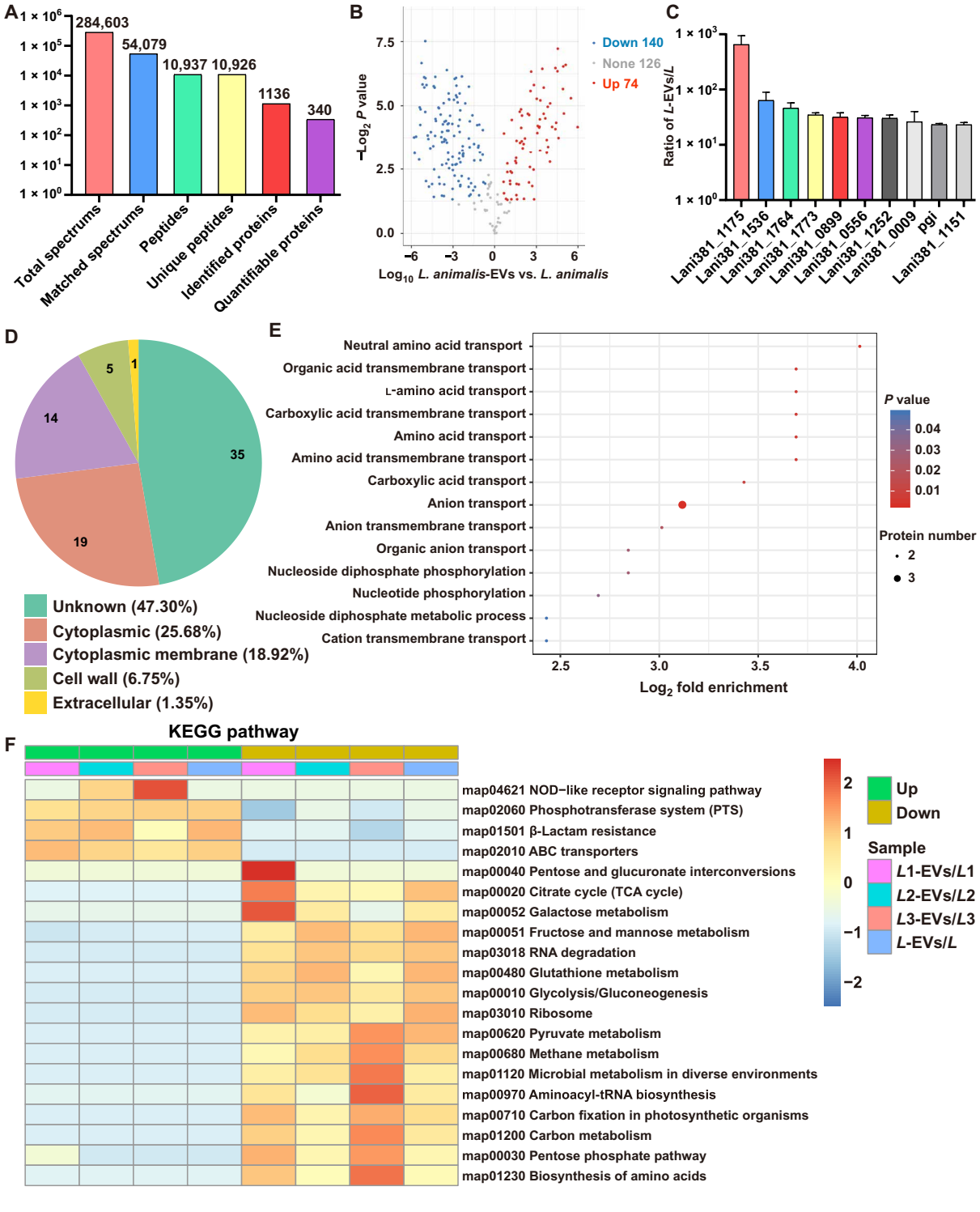

Fig. 6. Proteomic analysis of *L. animalis*-EVs and *L. animalis*. (**A**) Summary of tandem mass spectrometry (MS/MS) database search results for *L. animalis*-EVs and *L. animalis*. (**B**) Volcano plot showing the numbers of differentially expressed proteins between *L. animalis*-EVs and *L. animalis* with the cutoff of $P < 0.05$ and |fold change| ≥ 1.5. (**C**) The expression ratios of the top 10 most abundant proteins in *L. animalis*-EVs (*L*-EVs) relative to *L. animalis* (*L*). $n = 3$ per group. (**D**) GO annotation of the up-regulated proteins in *L. animalis*-EVs relative to *L. animalis* in terms of their subcellular localizations. (**E**) GO biological process enrichment analysis of the up-regulated proteins in *L. animalis*-EVs relative to *L. animalis*. (**F**) KEGG pathway enrichment analysis of the differentially expressed proteins in *L. animalis*-EVs relative to *L. animalis*.

domain (NOD)-like receptor signaling pathway, phosphotransferase system, β-lactam resistance, or adenosine triphosphate–binding cassette (ABC) transporters (Fig. 6F). These findings indicate that *L. animalis*-EVs are selectively enriched with various functional proteins.

DISCUSSION

Drugs in the GC family, such as MPS, dexamethasone, and hydrocortisone, have been widely used for immunosuppressive and anti-inflammatory purposes (*2*). However, GC use leads to a higher risk of many complications, such as ONFH and gut dysbiosis (*1*, *2*, *29*). ONFH is a progressive disease that often leads to femoral head collapse and hip joint dysfunction, which needs to debride dead bone and even requires total hip replacement (*1*, *2*). A study by Fukushima *et al.* (*30*) has reported that the systemic use of GC is the potential causative factor in 51% of atraumatic cases of ONFH in Japan. Cui *et al.* (*31*) have shown that 24.1% of patients in 6395 cases of ONFH in China are associated with GC administration. To date, however, the etiology of GC-induced ONFH has not been fully understood. Evidence increasingly indicates that the gastrointestinal tract can communicate with the skeleton via a gut-bone axis (*32*). It is known that intestinal calcium absorption is crucial for maintaining bone mineralization, whereas other factors such as GM and its metabolites also play important roles in regulating bone homeostasis (*11*–*13*, *32*). Here, we found that GM transfer from healthy mice by cohousing or direct colonization attenuated ONFH in GC-treated mice. Moreover, we found a potential etiologic link between reduced abundance of the gut bacterium *L. animalis* and the development of GC-induced ONFH because cohousing with healthy mice could rescue the significant reduction of *L. animalis* in GC-treated mice and direct supplementation of this bacterium was able to mitigate GC-induced ONFH. Last, we demonstrated that *L. animalis*-EVs could be transported to bone including the femoral head and prevent GC-induced ONFH in mice. Our study presents an unidentified mechanism in the pathogenesis of GC-induced ONFH and a new mode by which GM contacts with bone via transferring bacterial EVs to the femoral head.

GCs are powerful anti-inflammatory and immunosuppressive agents widely used for treating many inflammatory diseases. However, after administration of the bacteria-derived proinflammatory factor lipopolysaccharide (LPS), subsequent treatment with GCs can activate the production of various pro- or anti-inflammatory factors through Toll-like receptor 4 signaling and induce ONFH (*33*). Osteonecrosis may occur in patients and animals receiving long-term continuous GC therapy (*34*, *35*). It may also occur after short-term discontinuous exposure to high doses of GC (*34*, *35*). In acute stage of various diseases, shock therapy with large-dosage GC is usually used (*36*, *37*). Previous studies have shown that osteonecrosis is more frequent in patients and animals receiving continuous low-dose GC versus those treated with a discontinuous high-dosage regimen (*35*, *38*). In our study, GC-induced ONFH mouse models were generated by injection of MPS at the first 3 days in a week for 3 weeks, a discontinuous administration method reported by the research group led by C.-Q. Zhang (*39*, *40*). Our results showed that GC treatment by this method did not induce systemic and regular changes in various pro- or anti-inflammatory factors that have been reported to be overproduced in animals receiving GC combined with LPS, suggesting that ONFH induced by GC using our current method is not mainly associated with the dysregulation of inflammatory responses. The methods of GC administration may have different impacts on the inflammatory state of the gut-immune axis and the composition of GM. Future studies are required to investigate whether continuous GC administration can trigger different impacts on inflammatory factor production and GM composition compared with discontinuous administration, which will better interpret the different incidences of ONFH in recipients receiving continuous or discontinuous GC therapy.

In our study, we found that transplantation with GM from vehicle-treated healthy mice significantly prevented, but did not entirely abolish, the GC-induced detrimental effects on the femoral heads of MPS-treated mice. Many reasons may account for the lack of complete phenotypic recovery in these mice. First, the timing of GM harvest may be a factor affecting the outcome because our results showed that the bone-beneficial bacterium *L. animalis* in fecal microbiota was not only decreased after MPS treatment but also showed a trend of reduction in vehicle-treated healthy mice with the increase in observation period, which may be associated with the administration of vehicle or the increase in mouse age. Second, it may be because our currently used regimen for GM treatment is not the optimal one. We did not compare the effects on the femoral head of our currently used regimen for GM treatment with other administration regimens. Appropriate readjustment of the dosage, frequency, and total time of GM treatment may lead to a better outcome. Third, it may be due to the fact that GC can damage the femoral head through multiple mechanisms and that the GM from vehicle-treated healthy mice is not capable of completely blocking or rescuing the GC-induced profound deleterious effects on the femoral head. Our study also showed that GM from MPS-treated mice did not induce notable detrimental effects on femoral heads in the conventionally raised vehicle-treated healthy mice but could cause bone loss in the femoral heads of microbiota-depleted vehicle-treated control mice and MPS-treated ONFH mice, suggesting the interference of endogenous GM on the effects of GM transplantation. The timing of GM collection may also affect this result because GM composition changes with the duration of GC treatment. A limitation of our study is that we did not assess the effects of GM from the vehicle- or MPS-treated mice at other time points on bone phenotype in the femoral head of the conventionally raised mice.

Lactobacillus is a large genus belonging to the phylum Firmicutes, and many bacteria in the genus are commensal in human and animal gastrointestinal tracts (*41*). The health benefits of different species of *Lactobacillus* on the host have been extensively studied, including the promotion of bone health. Colonization with *Lactobacillus plantarum* strain WJL by oral gavage increases femur length in the germ-free mice (*12*). Oral administration of *L. rhamnosus* GG decreases inflammation and bone loss in leuprolide-induced sex steroid–deficient mice (*11*). *L. reuteri* 6475 can prevent bone loss in post-antibiotic– or ovariectomy (OVX)–induced osteoporotic mice (*42*, *43*) and enhance bone density in healthy mice (*44*). A clinical trial has determined the bone-protective effects of *L. reuteri* 6475 in older women with low bone mass (*45*). The intake of milk products fermented by *L. plantarum* A41, *Lactobacillus fermentum* SRK414, *Lactobacillus paracasei* NTU 101, or *L. plantarum* NTU 102 also increases bone mass in OVX rats (*46*, *47*). However, there are no reports on the role of *Lactobacillus* species in the maintenance of bone homeostasis in the femoral head.

Previous studies have shown that GC exposure leads to *Lactobacillus* reduction in fecal samples from people (*15*) and cecal contents from

rats (*16*), but the researchers have not further explored whether the alteration in *Lactobacillus* species is correlated with GC-induced complications, such as ONFH. Evidence in our study showed that GC treatment caused a decrease in *L. animalis* abundance in fecal microbiota of mice. As a member of *Lactobacillus*, *L. animalis* has not been studied extensively. The published literature on the function of *L. animalis* is mainly limited to its use as a starter culture (*48*), its ability to degrade oxalate (*49*), and its inhibitory effect on the growth of pathogenic bacteria (*50*). Here, we found that reduced abundance of *L. animalis* was associated with the development of GC-induced ONFH in mice, and oral treatment with *L. animalis* at the early stage of GC exposure effectively protected the mouse femoral head from GC-induced osteonecrosis. Our results uncover an unidentified function of *L. animalis* and further enrich the knowledge of *Lactobacillus*-dependent improvement of bone disease. A comprehensive overview of GM composition throughout the GC administration period will be beneficial for evaluating the dynamic changes in GM composition and for better interpreting our observations. Our study only used 16*S* rRNA gene sequencing to assess the changes in GM composition in mice at the last time of receiving GC administration and presented evidence of the dynamic alteration of *L. animalis* abundance during the GC treatment period using qRT-PCR. Note that we could not design and use a pair of primers exclusively specific to *L. animalis* for qRT-PCR because *L. animalis* shares very high similarities of 16*S* rRNA gene sequences with *Lactobacillus faecis*, *Lactobacillus apodeme*, and *Lactobacillus murinus* (*51*). Although these three species of bacteria were not detected in the mouse feces by 16*S* rRNA gene sequencing in our study, it will be better to further perform 16*S* rRNA gene sequencing to accurately assess the dynamic changes of bacterial community composition and *L. animalis* abundance in fecal microbiota throughout the entire period of GC treatment. Note that although *L. animalis* is commonly isolated from dog, pig, chicken, and mouse feces, this bacterium has not been reported as a prevalent microbe in the human gut (*48*, *50*), suggesting that *L. animalis* is not likely involved in the development of GC-induced ONFH in human patients. Nevertheless, *L. animalis* is detected in both human and animal milk (*52*, *53*), suggesting that this bone-beneficial bacterium is safe to consume and may contribute to the beneficial effects of milk consumption on bone health. In future studies, it will be worthwhile to determine whether *L. animalis* can be used as a probiotic bacterium for preventing GC-induced ONFH in human.

The mechanism through which GM exerts regulatory effects on bone is currently not well known. Evidence has shown that GM develops multiple ways to affect bone homeostasis. There exist gut bacteria that promote bone growth by facilitating mineral absorption or participating in the synthesis of substances useful to bone health, such as short-chain fatty acids and vitamins such as B and K (*32*, *47*). There are also gut bacteria that alter bone metabolism by interacting with the host immune cells and the regulation of anti- or proinflammatory factor production (*11*, *32*, *43*, *44*). In addition, bacterial components such as LPS may translocate across the gut endothelial barrier and into the circulation, where they can be transported to bone to induce inflammation and bone destruction (*32*). The secretion of bacterial EVs is another mechanism underlying the exchange of information between the GM and the host cells (*20*–*23*). Bacterial EVs selectively carry a variety of molecules (LPS, nucleic acids, proteins, etc.) from their parent bacteria and can travel a long distance to deliver these molecules to host cells, thus altering the function of the recipient cells (*20*–*23*).

In this study, we identified an EV-dependent regulatory mechanism by which gut *L. animalis* preserved bone and marrow structural integrity in the femoral head. After oral administration to GC-treated mice, *L. animalis*-EVs could enter the distant sites including the femoral head and trigger a series of beneficial effects, including enhancing blood vessel abundance, maintaining osteogenic activity, reducing cell apoptosis, and attenuating trabecular bone and marrow damage, thus protecting the mice from GC-induced ONFH. In healthy mice, *L. animalis*-EVs also improved trabecular bone microarchitecture in the femoral head. The direct regulatory effects of *L. animalis*-EVs on host cells are likely a major mechanism by which *L. animalis*-EVs induce benefits on femoral head, as *L. animalis*-EVs could directly enhance the angiogenic activity of endothelial cells, promote osteogenic differentiation of BMSCs, and suppress cell apoptosis. *L. animalis*-EVs were also able to increase the secretion of proangiogenic paracrine factors by endothelial cells and osteocytes, which may be another important mechanism by which *L. animalis*-EVs benefit microenvironment and bone health. Our results showed that *L. animalis*-EVs could protect various types of cells from GC-induced apoptosis, but a limitation of our study is that we did not determine which cells were the major cell type protected from apoptosis in mice after *L. animalis*-EV administration. Moreover, note that *L. animalis*-EVs at our currently used administration regimen could not entirely block the GC-induced detrimental effects on the cultured cells and mouse femoral heads. Further studies are required to determine the optimal dosage, frequency, and duration of *L. animalis*-EV treatment for preventing GC-induced cell damage and ONFH. In addition, currently, it remains unclear how bacterial EVs penetrate the intestinal mucus layer, cross the epithelial cell barrier, bypass the immune cells, and reach the host organs/tissues. Future studies are needed to explore the detailed mechanism by which *L. animalis*-EVs enter the distant organs/tissues including the bones of mice after oral administration. Our results showed that *L. animalis*-EVs were still maintained at a certain level after 72 hours of administration. It remains to be investigated how long it will take for the exogenously administered *L. animalis*-EVs to be entirely metabolized by the recipient mice.

The underlying molecular mechanism by which *L. animalis*-EVs protect against GC-induced ONFH may be the transfer of some proangiogenic, pro-osteogenic, and antiapoptotic proteins to endothelial cells and bone cells, as *L. animalis*-EVs were enriched with many functional proteins compared with *L. animalis* and could directly increase endothelial angiogenesis, augment BMSC osteogenesis, and inhibit cell apoptosis. However, the proteins that mediate the *L. animalis*-EV–induced benefits on the femoral head still require further determination. The proteomic changes in the femoral heads of the vehicle- or MPS-treated mice receiving *L. animalis*-EVs or their parent bacterium *L. animalis* treatment also warrant future investigation. Preosteoclasts can secrete platelet-derived growth factor–BB (PDGF-BB) to induce the generation of type H vessels and thereby increase bone formation (*54*). Peng *et al.* (*55*) have shown that GC exposure results in preosteoclast PDGF-BB reduction by inhibiting nuclear factor κB (NF-κB)–mediated *Pdgfb* transcription, which likely contributes to the inhibitory effects of GC on type H vessel formation and subsequent bone formation. In our study, we found that *L. animalis*-EVs were enriched with proteins involved in the NOD-like receptor signaling pathway. Since this signaling

can trigger the activation of NF-κB upon stimulation (*56*), the activation of NF-κB–mediated promotion of preosteoclast PDGF-BB production and subsequent type H vessel formation might be an indirect mechanism by which *L. animalis*-EVs attenuate the GC-induced reduction of blood vessel abundance in the femoral head, which still requires future exploration.

MATERIALS AND METHODS

Ethics statement

Experiments in this study were approved by the Ethical Review Board at Xiangya Hospital of Central South University (no. 202005422).

Cell culture

L. animalis ATCC 35046 (BNCC134981; BNBIO, Beijing, China) and *L. reuteri* ATCC PTA 6475 (ATCC, Manassas, VA, USA) were cultured in de Man Rogosa Sharp (MRS) broth (Solarbio, Beijing, China) with shaking (300 rpm) at 37°C in a microaerophilic chamber (88% N_2, 2% O_2, 5% CO_2, and 5% H_2; LAI-3T; Shanghai Longyue Instrument Equipment Co. Ltd., Shanghai, China). The bacterial concentration was assayed by counting the colony-forming units (CFUs) after plating overnight on MRS agar (Solarbio) or by testing the optical density (OD) of the bacterial solution at 600 nm with a microplate reader (Thermo Fisher Scientific, Waltham, USA). HMECs were immortalized cells derived from human dermal microvascular endothelium and obtained from ATCC (CRL-3243). MC3T3-E1 cells were derived from mouse calvaria and purchased from Procell (CL-0378; Wuhan, China). HMECs were grown in MCDB131 medium (Gibco, Grand Island, USA) with 1% GlutaMAX (Gibco), epidermal growth factor (10 ng/ml; PeproTech, Rocky Hill, USA), 1% penicillin-streptomycin (Solarbio), and 10% fetal bovine serum (FBS; Gibco). MC3T3-E1 cells were incubated in high-glucose Dulbecco's modified Eagle's medium (Gibco) with 1% penicillin-streptomycin and 10% FBS. MLO-Y4 cells were derived from mouse long bone and purchased from Procell (CL-0567). MLO-Y4 cells were cultured in α-minimum essential medium (α-MEM) (HyClone, Logan, USA) with 2.5% FBS, 2.5% calf serum (Gibco), and 1% penicillin-streptomycin. Primary BMSCs were harvested from the femurs and tibias of 2-month-old C57BL/6J male mice. These cells were cultured in α-MEM with 1% penicillin-streptomycin and 10% FBS. Cells were grown at 37°C with 5% CO_2.

Preparation and characterization of *L. animalis*-EVs

For isolation of *L. animalis*-EVs, *L. animalis* were incubated in fresh MRS broth for 3 days and then pelleted by sequential centrifugation at 2000*g* for 30 min and 10,000*g* for 30 min at 4°C. The culture supernatant was filtered by a 0.22-μm filter (Millipore, Billerica, USA) and then concentrated 100-fold by centrifugation at 4000*g* and 4°C in Amicon Ultra-15 Centrifugal Filter Units (100 kDa; Millipore). *L. animalis*-EVs were purified from the concentrated supernatant using OptiPrep density gradient centrifugation. Briefly, *L. animalis*-EVs (1.33 ml per tube) were added at the bottom of OptiPrep solution [6.67 ml per tube; 60% (w/v) iodixanol; Sigma-Aldrich, St. Louis, USA] in a polyallomer Beckman Coulter tube (38.5 ml), thus producing a 50% OptiPrep layer. Solutions of 40% (8 ml), 20% (8 ml), and 10% (7 ml) OptiPrep and 1 ml of PBS were sequentially and carefully added on the 50% OptiPrep layer to generate a discontinuous gradient. After centrifugation for 18 hours at 100,000*g* with a SW 32 Ti rotor (*k* factor, 204), 2 ml each of the OptiPrep density gradient fractions was obtained for nanoparticle tracking analysis to determine the EV-rich fractions (fractions 12 and 13). The EV-rich fractions were diluted with PBS to 30 ml and subjected to centrifugation for 3 hours at 100,000*g* and 4°C to pellet *L. animalis*-EVs. The obtained *L. animalis*-EVs were resuspended in PBS. A small volume of *L. animalis*-EVs was subjected to bacterial colony counting assay on MRS agar plate to ensure that there is no bacterial contamination. Protein contents of *L. animalis*-EVs were tested using a Pierce BCA protein assay kit (Thermo Fisher Scientific). The morphologies and diameters of *L. animalis*-EVs were assessed by a transmission electron microscope (Hitachi H-7650; Tokyo, Japan) and nanoparticle tracking analysis using a ZetaView nanoparticle tracking analyzer (Particle Metrix, Meerbusch, Germany). *L. animalis*-EVs were used immediately or stored at −80°C until downstream experiments.

Animals and treatments

Two- or 3-month-old C57BL/6J male mice mainly weighing 20 to 24 g were used in this study and randomly assigned to different treatment groups. Mice with body weight of <18 or >26 g or in poor physical condition before treatments were excluded from the experiments. All mice were maintained under specific pathogen–free conditions. To induce GC-induced ONFH, 3-month-old mice were intramuscularly injected with MPS (20 mg/kg per day; Pfizer, New York, USA) into the left thigh on the first 3 days of a week for 3 weeks. The mice given vehicle (DMSO) using the same treatment regimen served as the healthy controls. To assess the effects of cohousing on femoral head, the MPS- or vehicle-treated mice were cohoused with the age-matched male mice receiving vehicle or MPS. Cohousing was started at the first MPS or vehicle injection and continued for 6 weeks. The non-cohoused vehicle- or MPS-treated mice served as the negative control and positive control, respectively. Feces from the cohoused or non-cohoused vehicle- or MPS-treated mice were collected at 3 weeks after MPS injection for 16*S* rRNA gene sequencing. To assess the impact of fecal microbiota transplantation on femoral head, feces were collected from the mice at 3 weeks after vehicle or MPS treatment, and GM suspensions from the vehicle- or MPS-treated mice ($GM^{Vehicle}$ or GM^{MPS}) were prepared. For preparation of GM samples, feces were resuspended in PBS (100 mg of feces per 1 ml of PBS) and centrifuged at 500*g* for 1 min to collect the supernatant (GM suspension), followed by determining the numbers of bacteria using bacterial colony counting assay. The recipient conventionally raised or microbiota-depleted MPS- or vehicle-treated mice were fasted for 6 hours before treatment, and the GM suspension (2×10^8 CFU in 200 μl of PBS) or vehicle (200 μl of PBS) was administered into the fasted mice by oral gavage. GM transplantation was started at the first MPS or vehicle injection and conducted once a week for 6 weeks. For preparation of the microbiota-depleted mice before ONFH induction or vehicle treatment, 2-month-old mice were treated with a cocktail of broad-spectrum antibiotics (Solarbio) in their drinking water for 4 weeks as described previously (*28*). These antibiotics include bacitracin (1 mg/ml), gentamycin (170 mg/ml), ciprofloxacin (125 mg/ml), neomycin (100 mg/ml), penicillin (100 U/ml), metronidazole (100 mg/ml), ceftazidime (100 mg/ml), streptomycin (50 mg/ml), and vancomycin (50 mg/ml). To detect the influence of *L. animalis* and *L. animalis*-EVs on femoral head, the MPS- or vehicle-treated mice were orally administered with *L. animalis* (4×10^6 CFU in 200 μl of PBS), *L. animalis*-EVs (30 μg in 200 μl of PBS), or an equal volume of PBS once a week. For preventative treatment, these

interventions were started at the first MPS or vehicle administration. For therapeutic treatment, these interventions were conducted in mice that had received multiple injections of MPS for 3 weeks and been left for another 3 weeks. After 3 weeks of intervention, five mice in vehicle, vehicle + *L. animalis*-EVs, MPS, or MPS + *L. animalis*-EV treatment groups were sacrificed to detect the presence and abundance of *L. animalis*-EVs in the mouse femoral head. After 6 weeks of treatment, five mice in each group were anesthetized and subjected to angiography. The remaining mice were sacrificed after harvesting blood by eyeball enucleation. The femoral heads were obtained and processed for downstream analyses. Serum samples were obtained for analysis of the concentrations of inflammatory factors using the ELISA kits from MultiSciences (Hangzhou, China) or Elabscience (Wuhan, China).

μCT analysis

After being fixed in 4% paraformaldehyde (PFA) for 2 days, the femoral head samples were subjected to μCT scanning (voltage, 70 kV; current, 400 μA; x-ray tube potential, 55 kVp; integration time, 400 ms; and voxel size, 11.4 μm) by vivaCT 80 (SCANCO Medical AG, Bruttisellen, Switzerland). The region of interest included the whole volume of trabecular bones within the femoral head. The cortical shell was excluded from the analysis. Images of the femoral heads were reconstructed by NRecon, and the trabecular bones in the femoral head were analyzed by CTAn v1.11 to determine Tb. BV/TV, Tb. Th, Tb. N, and Tb. Sp.

Angiography

The mice were anesthetized, and the vasculature was flushed with normal saline through the left ventricle after the thoracic cavity was opened, followed by perfusion with 4% PFA and then Microfil MV-122 (Flow Tech, Carver, USA). The mice were placed overnight at 4°C, and the femoral heads were then obtained, fixed for 48 hours with 4% PFA, decalcified for 1 week using 0.5 M EDTA (Servicebio, Wuhan, China), and scanned by μCT. Total vessel volume within the femoral head was analyzed using CTAn v1.11.

Tissue staining assays

The femoral heads were embedded in paraffin after fixing with 4% PFA for 2 days, decalcification in 0.5 M EDTA for 1 week, dehydration using graded ethanol, and immersion in xylene. The paraffin-embedded femoral head samples were cut into 5-μm-thick sections and stained with H&E using reagents from Servicebio. Immunohistochemical staining for vascular marker CD31 and osteogenic marker OCN was performed as described previously (*18*, *27*). Anti-CD31 (GB113151), anti-OCN (GB11233), and the secondary antibody (GB23303) were obtained from Servicebio. Apoptotic cells were stained with a TUNEL detection kit (Servicebio). The sections were photographed with an Olympus CX31 microscope (Tokyo, Japan). The numbers of the CD31-, OCN-, or TUNEL-positive cells were measured with the Image-Pro Plus 6 software.

Preparation of antibodies targeting *L. animalis*-EVs

The preparation of polyclonal antibodies targeting *L. animalis*-EVs was conducted by FriendBio Technology (Wuhan, China). Briefly, two 3-month-old New Zealand male rabbits were subcutaneously injected with 500 μg of *L. animalis*-EVs (dissolved in 250 μl of PBS) for each rabbit after harvesting the preimmune serum (≥1 ml for each rabbit). The rabbits were then boosted four times with *L. animalis*-EVs (500 μg in 250 μl of PBS for each rabbit) at days 20, 35, 50, and 60 after the first injection. Nine days later, the serum samples (≥40 ml for each rabbit) were obtained to determine the titer of the antibodies targeting *L. animalis*-EVs using ELISA. The serum showing the highest titer of *L. animalis*-EV antibodies was selected for further experiment.

Tissue distribution of *L. animalis*-EVs

To trace the tissue distribution of *L. animalis*-EVs in mice after oral gavage, *L. animalis*-EVs were labeled with DiR (Santa Cruz Biotechnology, Santa Cruz, USA) or DiO (Invitrogen, Carlsbad, USA) as previously described (*1*) and then subjected to OptiPrep density gradient centrifugation using the procedures as described above to remove the redundant dye. The DiR- or DiO-labeled *L. animalis*-EVs (30 μg in 200 μl of PBS) were orally administered into the fasted MPS-treated mice by intragastric administration. The control MPS-treated mice were treated with 200 μl of PBS. Three, 24, or 72 hours later, all mice were sacrificed. The heart, brain, liver, spleen, lungs, gastrointestine, muscles, kidneys, femurs, tibias, and femoral heads from the mice treated with vehicle or DiR-labeled *L. animalis*-EVs were subjected to ex vivo fluorescent imaging with FMT-4000 (PerkinElmer, Waltham, USA). The femoral heads from the vehicle- or DiO-labeled *L. animalis*-EV–treated mice were fixed for 48 hours with ice-cold 4% PFA, decalcified for 72 hours with 0.5 M EDTA, dehydrated in 30% sucrose, and then embedded in Tissue-Tek optimal cutting temperature compound (Sakura Finetek, Torrance, USA). The samples were sliced into 14-μm-thick sections and stained with 4′,6-diamidino-2-phenylindole (DAPI; 0.5 μg/ml; Invitrogen). The fluorescent signals of DiO were detected using a Zeiss fluorescence microscope (Jena, Germany). To test whether *L. animalis*-EVs could be transported to the femoral head using the antibodies targeting these EVs, the femoral heads from the vehicle-, vehicle + *L. animalis*-EV–, MPS-, or MPS + *L. animalis*-EV–treated mice were collected and processed as described above. The femoral head sections (14 μm thick) were blocked with 3% donkey serum for 30 min, incubated overnight at 4°C with the rabbit preimmune serum (negative control) or the serum containing the antibodies targeting *L. animalis*-EVs, and then incubated with the secondary antibody (GB23303; Servicebio) at room temperature for 2 hours. After being counterstained with DAPI, the sections were detected under a fluorescence microscope, and the mean intensity of the *L. animalis*-EV–positive areas was quantified.

L. animalis-EV uptake assay

The DiO-labeled *L. animalis*-EVs were prepared using the procedures described previously (*1*) and incubated with different cell types for 3 hours at 37°C. The recipient cells were then washed with PBS, stained with DAPI, and observed under a Zeiss fluorescence microscope.

Tube formation assay

The growth factor–reduced Matrigel (BD Biosciences, San Jose, USA) was plated in a 96-well plate for 30 min at 37°C, and HMECs (8×10^3 cells per well) were seeded on Matrigel. To assess the direct effects of *L. animalis*-EVs and *L. reuteri*-EVs on endothelial angiogenesis, HMECs were treated with vehicle, vehicle + *L. animalis*-EVs (10 μg/ml), vehicle + *L. reuteri*-EVs (10 μg/ml), MPS (160 μM), MPS + *L. animalis*-EVs (2.5 to 20 μg/ml), or MPS + *L. reuteri*-EVs (10 μg/ml). To assess whether *L. animalis*-EVs could indirectly regulate the angiogenic activity of endothelial cells by stimulating cells to secrete proangiogenic factors, HMECs, MLO-Y4, MC3T3-E1,

and BMSCs were incubated with *L. animalis*-EVs (10 μg/ml) or vehicle for 6 hours. The CM was then replaced with fresh complete CM, and the cells were cultured for another 24 hours. The CMs of the vehicle- or *L. animalis*-EV–pretreated cells were harvested and subjected to centrifugation (300*g* for 10 min and 2000*g* for 30 min) to remove dead cells and debris. After determining the protein concentration of CM using a BCA protein assay kit, the effects of different cell-derived CM on tube formation of HMECs were assessed at the final dose of 10 μg/ml. HMECs treated with the uncultured complete medium of the above-described cells served as the negative controls. After receiving the different treatments above at 37°C for 6 hours, HMECs were photographed using an optical microscope (AE2000; Motic, Xiamen, China). Total loops and total tube length were measured using the Image-Pro Plus 6.0 software.

Osteogenic differentiation assay

When BMSCs were grown to 80% confluence, the CM (complete α-MEM: α-MEM + 10% FBS + 1% penicillin-streptomycin) was changed to the osteogenic induction medium (Cyagen Biosciences, Guangzhou, China) supplemented with vehicle, vehicle + *L. animalis*-EVs (10 μg/ml), vehicle + *L. reuteri*-EVs (10 μg/ml), MPS (160 μM), MPS + *L. animalis*-EVs (10 μg/ml), or MPS + *L. reuteri*-EVs (10 μg/ml). Half of the medium with the supplements was replenished every 2 days. The cells were stained with ARS solution (Solarbio) at 10 days after induction. Images were obtained, and the percentage of the ARS-positive areas was measured with the Image-Pro Plus 6 software.

CCK-8 assay

HMECs, MLO-Y4, MC3T3-E1, and BMSCs (5×10^3 cells per well) were seeded in a 96-well plate and cultured overnight in complete medium. After 24 hours of culture in serum-free medium, the medium was changed to fresh serum-free medium with vehicle, vehicle + *L. animalis*-EVs (10 μg/ml), vehicle + *L. reuteri*-EVs (10 μg/ml), MPS (160 μM), MPS + *L. animalis*-EVs (10 μg/ml), or MPS + *L. reuteri*-EVs (10 μg/ml). After 24 hours of culture at 37°C, the cells were incubated for another 3 hours in fresh medium containing CCK-8 solution (7Sea Biotech, Shanghai, China). The OD at 450 nm was assessed with a microplate reader (Varioskan LUX; Thermo Fisher Scientific). The survival/growth rate was calculated as described in our previous study (*1*).

Cell apoptosis assay

HMECs, MLO-Y4, MC3T3-E1, and BMSCs (5×10^4 cells per well in a 48-well plate) were cultured overnight in complete medium and then in serum-free medium for another 24 hours. The medium was then replaced with fresh serum-free medium containing vehicle, vehicle + *L. animalis*-EVs (10 μg/ml), vehicle + *L. reuteri*-EVs (10 μg/ml), MPS (160 μM), MPS + *L. animalis*-EVs (10 μg/ml), or MPS + *L. reuteri*-EVs (10 μg/ml). Twenty-four hours later, cell apoptosis was tested using a TUNEL detection kit (Yearend Biotech, Shanghai, China). The ratio of apoptotic cells was quantified.

16*S* rRNA gene sequencing

Total genomic DNA was extracted from the feces of cohoused or non-cohoused mice receiving vehicle or MPS treatment for 3 weeks and processed for 16*S* rRNA gene sequencing by Genesky Biotechnologies Inc. (Shanghai, China) for the relative and absolute quantification of microbiota abundance. Briefly, the DNA samples were mixed with artificial spike-in reference sequences after quality detection and subjected to amplification of V3V4 variable regions of bacteria 16*S* rRNA gene. Sample-specific index sequences were added to the DNA pools, followed by library quantification, pooling, and quality check. Libraries were sequenced on Illumina MiSeq Sequencer (Illumina, USA) using a 2 × 250–base pair (bp) double-ended sequencing technology. Raw reads were trimmed using the tools TrimGalore, Mothur, and Usearch to remove the low-quality sequences (quality score < 20), adaptor sequences, primer sequences, shorter sequences (<100 bp), and sequences with high base error rate (>2) to obtain the clean reads with high quality and credibility. Sequences with high similarity (>97%) were clustered into OTUs using the UPARSE algorithm. The spike-in DNA sequences were filtered out, and the copy number of spike-in OTU in each sample was counted. A standard curve of read count of each OTU versus spike-in DNA copy number of each sample was generated. The absolute copy number of each OTU was calculated on the basis of the standard curve and then adjusted on the basis of the estimated rRNA operon copy number according to the rrnDB database. The taxonomies of each OTU were annotated by the software Mothur with a confidence threshold of 80%. The microbial community richness was analyzed using the Chao1 and ACE estimators.

qRT-PCR analysis

Total genomic DNA was extracted from the feces of mice injected with vehicle or MPS at the first 3 days in a week for 1, 2, and 3 weeks with a TIANamp stool DNA kit (Tiangen, Beijing, China). Total DNA (500 ng) was used for qRT-PCR amplification. Relative DNA levels were calculated by the comparative Ct ($2^{-\Delta\Delta CT}$) method using the bacterium universal 16*S* rRNA primers for normalization. The sequences of the universal primers and the primers for the variable regions of the 16*S* rRNA gene sequence of *L. animalis* were as follows: universal primers, 5′-ACTCCTACGGGAGGCAGCAGT-3′ (forward) and 5′-ATTACCGCGGCTGCTGGC-3′ (reverse) and *L. animalis*, 5′-CTCACCGATAAAGAGTTGAG-3′ (forward) and 5′-CCATGCGGTAACTATGGTTA-3′ (reverse).

Proteomic analysis

Three biological replicate samples for *L. animalis*-EVs (*L*1-EVs, *L*2-EVs, and *L*3-EVs) and *L. animalis* (*L*1, *L*2, and *L*3) were obtained and processed for label-free proteomic analysis by Jingjie PTM BioLab (Hangzhou, China). Briefly, total proteins of *L. animalis*-EVs and *L. animalis* were extracted and digested overnight with trypsin at a trypsin-to-protein mass ratio of 1:50. The tryptic peptides were dissolved in 0.1% formic acid and 2% acetonitrile, followed by chromatographic separation with a gradient elution of 0.1% formic acid and 90% acetonitrile at a flow rate of 500 nl/min on an EASY-nLC 1000 ultrahigh-performance liquid chromatography system. The resulting peptides were subjected to nanospray ionization and then analyzed by tandem mass spectrometry (MS/MS) in Q Exactive Plus (Thermo Fisher Scientific). MaxQuant search engine (v.1.5.2.8) was used to process the resulting MS/MS data. Tandem mass spectra were searched against UniProt–*L. animalis* database concatenated with reverse decoy database. False discovery rate at the protein and peptide-to-spectrum match levels was adjusted to <1%. GO analysis was conducted to annotate all the identified proteins. Functional enrichment analyses based on GO and KEGG pathways were performed for better understanding of the function of the differentially expressed proteins ($P < 0.05$; $|\text{fold change}| \geq 1.5$) between *L. animalis*-EVs and *L. animalis*.

Statistical analysis

Data are shown as means ± SD. Student's *t* test (unpaired, two-tailed) was used for analyzing the differences between two groups. Multiple-group comparisons were performed using one- or two-way analysis of variance (ANOVA) followed by Bonferroni post hoc test. $P < 0.05$ was considered statistically significant, with $^{*}P < 0.05$, $^{**}P < 0.01$, and $^{**}P < 0.001$.

SUPPLEMENTARY MATERIALS

Supplementary material for this article is available at https://science.org/doi/10.1126/sciadv.abg8335

View/request a protocol for this paper from *Bio-protocol*.

REFERENCES AND NOTES

1. C. Y. Chen, W. Du, S. S. Rao, Y. J. Tan, X. K. Hu, M. J. Luo, Q. F. Ou, P. F. Wu, L. M. Qing, Z. M. Cao, H. Yin, T. Yue, C. H. Zhan, J. Huang, Y. Zhang, Y. W. Liu, Z. X. Wang, Z. Z. Liu, J. Cao, J. H. Liu, C. G. Hong, Z. H. He, J. X. Yang, S. Y. Tang, J. Y. Tang, H. Xie, Extracellular vesicles from human urine-derived stem cells inhibit glucocorticoid-induced osteonecrosis of the femoral head by transporting and releasing pro-angiogenic DMBT1 and anti-apoptotic TIMP1. *Acta Biomater.* **111**, 208–220 (2020).
2. M. Zaidi, L. Sun, L. J. Robinson, I. L. Tourkova, L. Liu, Y. Wang, L. L. Zhu, X. Liu, J. Li, Y. Peng, G. Yang, X. Shi, A. Levine, J. Iqbal, B. B. Yaroslavskiy, C. Isales, H. C. Blair, ACTH protects against glucocorticoid-induced osteonecrosis of bone. *Proc. Natl. Acad. Sci. U.S.A.* **107**, 8782–8787 (2010).
3. X. Wu, W. Sun, M. Tan, Noncoding RNAs in steroid-induced osteonecrosis of the femoral head. *Biomed. Res. Int.* **2019**, 8140595 (2019).
4. R. S. Weinstein, R. L. Jilka, A. M. Parfitt, S. C. Manolagas, Inhibition of osteoblastogenesis and promotion of apoptosis of osteoblasts and osteocytes by glucocorticoids. Potential mechanisms of their deleterious effects on bone. *J. Clin. Invest.* **102**, 274–282 (1998).
5. X. Yao, S. Yu, X. Jing, J. Guo, K. Sun, F. Guo, Y. Ye, PTEN inhibitor VO-OHpic attenuates GC-associated endothelial progenitor cell dysfunction and osteonecrosis of the femoral head via activating Nrf2 signaling and inhibiting mitochondrial apoptosis pathway. *Stem Cell Res Ther* **11**, 140 (2020).
6. M. A. Kerachian, C. Seguin, E. J. Harvey, Glucocorticoids in osteonecrosis of the femoral head: A new understanding of the mechanisms of action. *J. Steroid Biochem. Mol. Biol.* **114**, 121–128 (2009).
7. N. M. Delzenne, A. M. Neyrinck, P. D. Cani, Modulation of the gut microbiota by nutrients with prebiotic properties: Consequences for host health in the context of obesity and metabolic syndrome. *Microb. Cell Factories* **10** (Suppl 1), S10 (2011).
8. C. Chen, E. H. Ahn, S. S. Kang, X. Liu, A. Alam, K. Ye, Gut dysbiosis contributes to amyloid pathology, associated with C/EBPβ/AEP signaling activation in Alzheimer's disease mouse model. *Sci. Adv.* **6**, eaba0466 (2020).
9. A. Lavelle, H. Sokol, Gut microbiota-derived metabolites as key actors in inflammatory bowel disease. *Nat. Rev. Gastroenterol. Hepatol.* **17**, 223–237 (2020).
10. A. Biragyn, L. Ferrucci, Gut dysbiosis: A potential link between increased cancer risk in ageing and inflammaging. *Lancet Oncol.* **19**, e295–e304 (2018).
11. J. Y. Li, B. Chassaing, A. M. Tyagi, C. Vaccaro, T. Luo, J. Adams, T. M. Darby, M. N. Weitzmann, J. G. Mulle, A. T. Gewirtz, R. M. Jones, R. Pacifici, Sex steroid deficiency-associated bone loss is microbiota dependent and prevented by probiotics. *J. Clin. Invest.* **126**, 2049–2063 (2016).
12. M. Schwarzer, K. Makki, G. Storelli, I. Machuca-Gayet, D. Srutkova, P. Hermanova, M. E. Martino, S. Balmand, T. Hudcovic, A. Heddi, J. Rieusset, H. Kozakova, H. Vidal, F. Leulier, Lactobacillus plantarum strain maintains growth of infant mice during chronic undernutrition. *Science* **351**, 854–857 (2016).
13. K. Sjogren, C. Engdahl, P. Henning, U. H. Lerner, V. Tremaroli, M. K. Lagerquist, F. Backhed, C. Ohlsson, The gut microbiota regulates bone mass in mice. *J. Bone Miner. Res.* **27**, 1357–1367 (2012).
14. X. Wei, S. Pushalkar, C. Estilo, C. Wong, A. Farooki, M. Fornier, G. Bohle, J. Huryn, Y. Li, S. Doty, D. Saxena, Molecular profiling of oral microbiota in jawbone samples of bisphosphonate-related osteonecrosis of the jaw. *Oral Dis.* **18**, 602–612 (2012).
15. D. Qiu, Z. Xia, J. Deng, X. Jiao, L. Liu, J. Li, Glucorticoid-induced obesity individuals have distinct signatures of the gut microbiome. *Biofactors* **45**, 892–901 (2019).
16. T. Wu, L. Yang, J. Jiang, Y. Ni, J. Zhu, X. Zheng, Q. Wang, X. Lu, Z. Fu, Chronic glucocorticoid treatment induced circadian clock disorder leads to lipid metabolism and gut microbiota alterations in rats. *Life Sci.* **192**, 173–182 (2018).
17. J. Tulkens, G. Vergauwen, J. Van Deun, E. Geeurickx, B. Dhondt, L. Lippens, M. A. De Scheerder, I. Miinalainen, P. Rappu, B. G. De Geest, K. Vandecasteele, D. Laukens, L. Vandekerckhove, H. Denys, J. Vandesompele, O. De Wever, A. Hendrix, Increased levels of systemic LPS-positive bacterial extracellular vesicles in patients with intestinal barrier dysfunction. *Gut* **69**, 191–193 (2020).
18. H. Yin, C. Y. Chen, Y. W. Liu, Y. J. Tan, Z. L. Deng, F. Yang, F. Y. Huang, C. Wen, S. S. Rao, M. J. Luo, X. K. Hu, Z. Z. Liu, Z. X. Wang, J. Cao, H. M. Liu, J. H. Liu, T. Yue, S. Y. Tang, H. Xie, Synechococcus elongatus PCC7942 secretes extracellular vesicles to accelerate cutaneous wound healing by promoting angiogenesis. *Theranostics* **9**, 2678–2693 (2019).
19. Y. Zhang, X. Jin, J. Liang, Y. Guo, G. Sun, X. Zeng, H. Yin, Extracellular vesicles derived from ODN-stimulated macrophages transfer and activate Cdc42 in recipient cells and thereby increase cellular permissiveness to EV uptake. *Sci. Adv.* **5**, eaav1564 (2019).
20. S. K. Vanaja, A. J. Russo, B. Behl, I. Banerjee, M. Yankova, S. D. Deshmukh, V. A. Rathinam, Bacterial outer membrane vesicles mediate cytosolic localization of LPS and caspase-11 activation. *Cell* **165**, 1106–1119 (2016).
21. L. Brown, J. M. Wolf, R. Prados-Rosales, A. Casadevall, Through the wall: Extracellular vesicles in Gram-positive bacteria, mycobacteria and fungi. *Nat. Rev. Microbiol.* **13**, 620–630 (2015).
22. J. H. Liu, C. Y. Chen, Z. Z. Liu, Z. W. Luo, S. S. Rao, L. Jin, T. F. Wan, T. Yue, Y. J. Tan, H. Yin, F. Yang, F. Y. Huang, J. Guo, Y. Y. Wang, K. Xia, J. Cao, Z. X. Wang, C. G. Hong, M. J. Luo, X. K. Hu, Y. W. Liu, W. Du, J. Luo, Y. Hu, Y. Zhang, J. Huang, H. M. Li, B. Wu, H. M. Liu, T. H. Chen, Y. X. Qian, Y. Y. Li, S. K. Feng, Y. Chen, L. Y. Qi, R. Xu, S. Y. Tang, H. Xie, Extracellular vesicles from child gut microbiota enter into bone to preserve bone mass and strength. *Adv. Sci.* **8**, 2004831 (2021).
23. Y. Choi, Y. Kwon, D. K. Kim, J. Jeon, S. C. Jang, T. Wang, M. Ban, M. H. Kim, S. G. Jeon, M. S. Kim, C. S. Choi, Y. K. Jee, Y. S. Gho, S. H. Ryu, Y. K. Kim, Gut microbe-derived extracellular vesicles induce insulin resistance, thereby impairing glucose metabolism in skeletal muscle. *Sci. Rep.* **5**, 15878 (2015).
24. T. Su, R. Liu, A. Lee, Y. Long, L. Du, S. Lai, X. Chen, L. Wang, J. Si, C. Owyang, S. Chen, Altered intestinal microbiota with increased abundance of prevotella is associated with high risk of diarrhea-predominant irritable bowel syndrome. *Gastroenterol. Res. Pract.* **2018**, 6961783 (2018).
25. L. V. Blanton, M. R. Charbonneau, T. Salih, M. J. Barratt, S. Venkatesh, O. Ilkaveya, S. Subramanian, M. J. Manary, I. Trehan, J. M. Jorgensen, Y. M. Fan, B. Henrissat, S. A. Leyn, D. A. Rodionov, A. L. Osterman, K. M. Maleta, C. B. Newgard, P. Ashorn, K. G. Dewey, J. I. Gordon, Gut bacteria that prevent growth impairments transmitted by microbiota from malnourished children. *Science* **351**, eaad3311 (2016).
26. A. Sivan, L. Corrales, N. Hubert, J. B. Williams, K. Aquino-Michaels, Z. M. Earley, F. W. Benyamin, Y. M. Lei, B. Jabri, M. L. Alegre, E. B. Chang, T. F. Gajewski, Commensal Bifidobacterium promotes antitumor immunity and facilitates anti-PD-L1 efficacy. *Science* **350**, 1084–1089 (2015).
27. C. Y. Chen, S. S. Rao, Y. J. Tan, M. J. Luo, X. K. Hu, H. Yin, J. Huang, Y. Hu, Z. W. Luo, Z. Z. Liu, Z. X. Wang, J. Cao, Y. W. Liu, H. M. Li, Y. Chen, W. Du, J. H. Liu, Y. Zhang, T. H. Chen, H. M. Liu, B. Wu, T. Yue, Y. Y. Wang, K. Xia, P. F. Lei, S. Y. Tang, H. Xie, Extracellular vesicles from human urine-derived stem cells prevent osteoporosis by transferring CTHRC1 and OPG. *Bone Res.* **7**, 18 (2019).
28. G. Li, C. Xie, S. Lu, R. G. Nichols, Y. Tian, L. Li, D. Patel, Y. Ma, C. N. Brocker, T. Yan, K. W. Krausz, R. Xiang, O. Gavrilova, A. D. Patterson, F. J. Gonzalez, Intermittent fasting promotes white adipose browning and decreases obesity by shaping the gut microbiota. *Cell Metab.* **26**, 672–685.e4 (2017).
29. X. Xie, Q. Xiao, Z. Xiong, C. Yu, J. Zhou, Z. Fu, Crocin-I ameliorates the disruption of lipid metabolism and dysbiosis of the gut microbiota induced by chronic corticosterone in mice. *Food Funct.* **10**, 6779–6791 (2019).
30. W. Fukushima, M. Fujioka, T. Kubo, A. Tamakoshi, M. Nagai, Y. Hirota, Nationwide epidemiologic survey of idiopathic osteonecrosis of the femoral head. *Clin. Orthop. Relat. Res.* **468**, 2715–2724 (2010).
31. L. Cui, Q. Zhuang, J. Lin, J. Jin, K. Zhang, L. Cao, J. Lin, S. Yan, W. Guo, W. He, F. Pei, Y. Zhou, X. Weng, Multicentric epidemiologic study on six thousand three hundred and ninety five cases of femoral head osteonecrosis in China. *Int. Orthop.* **40**, 267–276 (2016).
32. D. Quach, R. A. Britton, Gut microbiota and bone health. *Adv. Exp. Med. Biol.* **1033**, 47–58 (2017).
33. S. Okazaki, Y. Nishitani, S. Nagoya, M. Kaya, T. Yamashita, H. Matsumoto, Femoral head osteonecrosis can be caused by disruption of the systemic immune response via the Toll-like receptor 4 signalling pathway. *Rheumatology* **48**, 227–232 (2008).
34. R. S. Weinstein, Glucocorticoid-induced osteonecrosis. *Endocrine* **41**, 183–190 (2012).
35. L. Yang, K. Boyd, S. C. Kaste, L. Kamdem Kamdem, R. J. Rahija, M. V. Relling, A mouse model for glucocorticoid-induced osteonecrosis: Effect of a steroid holiday. *J. Orthop. Res.* **27**, 169–175 (2009).
36. H. M. Liu, C. Dong, Y. Z. Zhang, Y. Y. Tian, H. X. Chen, S. Zhang, N. Li, P. Gu, Clinical and imaging features of spinal cord type of neuro Behçet disease: A case report and systematic review. *Medicine* **96**, e7958 (2017).
37. T. A. El Gamal, A. El-Bakoury, A. Hawkins, M. E. A. T. Mussa, T. E. A. Sweed, S. E. S. Ansara, Bilateral osteonecrosis of the femoral and humeral heads after short term corticosteroid therapy. A case study. *Ortop. Traumatol. Rehabil.* **18**, 187–190 (2016).
38. L. A. Mattano Jr., M. Devidas, J. B. Nachman, H. N. Sather, S. P. Hunger, P. G. Steinherz, P. S. Gaynon, N. L. Seibel, Effect of alternate-week versus continuous dexamethasone

scheduling on the risk of osteonecrosis in paediatric patients with acute lymphoblastic leukaemia: Results from the CCG-1961 randomised cohort trial. *Lancet Oncol.* **13**, 906–915 (2012).
39. S. C. Tao, T. Yuan, B. Y. Rui, Z. Z. Zhu, S. C. Guo, C. Q. Zhang, Exosomes derived from human platelet-rich plasma prevent apoptosis induced by glucocorticoid-associated endoplasmic reticulum stress in rat osteonecrosis of the femoral head via the Akt/Bad/Bcl-2 signal pathway. *Theranostics* **7**, 733–750 (2017).
40. S. C. Guo, S. C. Tao, W. J. Yin, X. Qi, J. G. Sheng, C. Q. Zhang, Exosomes from human synovial-derived mesenchymal stem cells prevent glucocorticoid-induced osteonecrosis of the femoral head in the rat. *Int. J. Biol. Sci.* **12**, 1262–1272 (2016).
41. D. Y. Park, W. J. Lee, I. H. Jang, W. J. Lee, Got Lactobacillus? Commensals power growth. *Cell Host Microbe* **18**, 388–390 (2015).
42. J. D. Schepper, F. L. Collins, N. D. Rios-Arce, S. Raehtz, L. Schaefer, J. D. Gardinier, R. A. Britton, N. Parameswaran, L. R. McCabe, Probiotic Lactobacillus reuteri prevents postantibiotic bone loss by reducing intestinal dysbiosis and preventing barrier disruption. *J. Bone Miner. Res.* **34**, 681–698 (2019).
43. R. A. Britton, R. Irwin, D. Quach, L. Schaefer, J. Zhang, T. Lee, N. Parameswaran, L. R. McCabe, Probiotic L. reuteri treatment prevents bone loss in a menopausal ovariectomized mouse model. *J. Cell. Physiol.* **229**, 1822–1830 (2014).
44. F. L. Collins, N. D. Rios-Arce, J. D. Schepper, A. D. Jones, L. Schaefer, R. A. Britton, L. R. McCabe, N. Parameswaran, Beneficial effects of Lactobacillus reuteri 6475 on bone density in male mice is dependent on lymphocytes. *Sci. Rep.* **9**, 14708 (2019).
45. A. G. Nilsson, D. Sundh, F. Bäckhed, M. Lorentzon, Lactobacillus reuteri reduces bone loss in older women with low bone mineral density: A randomized, placebo-controlled, double-blind, clinical trial. *J. Intern. Med.* **284**, 307–317 (2018).
46. C. S. Lee, J. Y. Kim, B. K. Kim, I. O. Lee, N. H. Park, S. H. Kim, Lactobacillus-fermented milk products attenuate bone loss in an experimental rat model of ovariectomy-induced post-menopausal primary osteoporosis. *J. Appl. Microbiol.* **130**, 2041–2062 (2020).
47. S. S. Chiang, T. M. Pan, Antiosteoporotic effects of Lactobacillus -fermented soy skim milk on bone mineral density and the microstructure of femoral bone in ovariectomized mice. *J. Agric. Food Chem.* **59**, 7734–7742 (2011).
48. S. Ruiz-Moyano, A. Martín, M. J. Benito, F. P. Nevado, M. de Guía Córdoba, Screening of lactic acid bacteria and bifidobacteria for potential probiotic use in Iberian dry fermented sausages. *Meat Sci.* **80**, 715–721 (2008).
49. C. Murphy, S. Murphy, F. O'Brien, M. O'Donoghue, T. Boileau, G. Sunvold, G. Reinhart, B. Kiely, F. Shanahan, L. O'Mahony, Metabolic activity of probiotics-oxalate degradation. *Vet. Microbiol.* **136**, 100–107 (2009).
50. C. F. Lin, M. Y. Lin, C. N. Lin, M. T. Chiou, J. W. Chen, K. C. Yang, M. C. Wu, Potential probiotic of Lactobacillus strains isolated from the intestinal tracts of pigs and feces of dogs with antibacterial activity against multidrug-resistant pathogenic bacteria. *Arch. Microbiol.* **202**, 1849–1860 (2020).
51. A. Endo, T. Irisawa, Y. Futagawa-Endo, S. Salminen, M. Ohkuma, L. Dicks, Lactobacillus faecis sp. nov., isolated from animal faeces. *Int. J. Syst. Evol. Microbiol.* **63**, 4502–4507 (2013).
52. R. Albesharat, M. A. Ehrmann, M. Korakli, S. Yazaji, R. F. Vogel, Phenotypic and genotypic analyses of lactic acid bacteria in local fermented food, breast milk and faeces of mothers and their babies. *Syst. Appl. Microbiol.* **34**, 148–155 (2011).
53. R. Martín, M. Olivares, M. Pérez, J. Xaus, C. Torre, L. Fernández, J. M. Rodríguez, Identification and evaluation of the probiotic potential of lactobacilli isolated from canine milk. *Vet. J.* **185**, 193–198 (2010).
54. H. Xie, Z. Cui, L. Wang, Z. Xia, Y. Hu, L. Xian, C. Li, L. Xie, J. Crane, M. Wan, G. Zhen, Q. Bian, B. Yu, W. Chang, T. Qiu, M. Pickarski, L. T. Duong, J. J. Windle, X. Luo, E. Liao, X. Cao, PDGF-BB secreted by preosteoclasts induces angiogenesis during coupling with osteogenesis. *Nat. Med.* **20**, 1270–1278 (2014).
55. Y. Peng, S. Lv, Y. Li, J. Zhu, S. Chen, G. Zhen, X. Cao, S. Wu, J. L. Crane, Glucocorticoids disrupt skeletal angiogenesis through transrepression of NF-κB-mediated preosteoclast pdgfb transcription in young mice. *J. Bone Miner. Res.* **35**, 1188–1202 (2020).
56. I. Tattoli, L. A. Carneiro, M. Jéhanno, J. G. Magalhaes, Y. Shu, D. J. Philpott, D. Arnoult, S. E. Girardin, NLRX1 is a mitochondrial NOD-like receptor that amplifies NF-kappaB and JNK pathways by inducing reactive oxygen species production. *EMBO Rep.* **9**, 293–300 (2008).

Acknowledgments

Funding: This work was supported by the National Natural Science Foundation of China (grant nos. 81871822, 82072504, 81670807, 81522012, 81702237, and 81974127), the Science and Technology Innovation Program of Hunan Province (grant no. 2020RC4008), the Science and Technology Plan Project of Hunan Province (grant nos. 2017XK2039 and 2018RS3029), Non-profit Central Research Institute Fund of Chinese Academy of Medical Sciences (grant no. 2019-RC-HL-024), the Special Funding for the Construction of Innovative Provinces in Hunan (grant nos. 2019SK2301 and 2020SK3002), the Innovation Driven Project of Central South University (grant no. 2019CX014), the Hunan Province Natural Science Foundation of China (grant no. 2020JJ5883), and the Free Exploration Program of Central South University (grant no. 502221901). **Author contributions:** H.X. and C.-Y.C. designed this study and wrote the manuscript. C.-Y.C., S.-S.R., T.Y., Y.-J.T., H.Y., L.-J.C., M.-J.L., Z.W., Y.-Y.W., C.-G.H., Y.-X.Q., Z.-H.H., and F.-Y.H. performed the experiments and/or analyzed the data. C.-Y.C. and S.-S.R. prepared the figures. J.-H.L., F.Y., and S.-Y.T. provided technical support. **Competing interests:** The authors declare that they have no competing interests. **Data and materials availability:** All data needed to evaluate the conclusions in the paper are present in the paper and/or the Supplementary Materials.

Submitted 30 January 2021
Accepted 24 February 2022
Published 13 April 2022
10.1126/sciadv.abg8335